An optogenetic method for interrogating YAP1 and TAZ nuclear-cytoplasmic shuttling

Anna M. Dowbaj, Robert P. Jenkins, Klaus Hahn, Marco Montagner, Erik Sahai

Abstract

The shuttling of transcription factors and transcriptional regulators in and out of the nucleus is central to the regulation of many biological processes. Here we describe a new method for studying the rates of nuclear entry and exit of transcriptional regulators. A photo-responsive AsLOV (*Avena sativa* Light Oxygen Voltage) domain is used to sequester the transcriptional regulators, YAP1 and TAZ/WWTR1, on the surface of mitochondria. Illumination with blue light is used to release fluorophore-tagged YAP1 and TAZ from mitochondria and their entry into the nucleus can be observed. Cessation of blue light illumination leads to re-sequestration on the surface of mitochondria. This method generates three distinct curves that are then used to fit ordinary differential equations for the rates of nuclear entry and exit. Using this method, we demonstrate that phosphorylation of YAP1 on sites of canonical regulation by LATS1/2 enhances its rate of nuclear export. Moreover, we provide evidences that YAP1 import and export rates, despite high intercellular variability, are correlated within the same cell. Interestingly, the ratio of import and export rates correlated with nuclear-cytoplasmic (NC) distribution of YAP1 and TAZ proteins at steady state.

Introduction

Rapid regulation of cellular processes in space and time is mostly achieved either by switching on inactive proteins in the correct location, or by recruiting proteins at the appropriate subcellular compartment at the right time. Compartmentalisation is a fundamental feature of eukaryotic cells and numerous membrane bound organelles contribute to sub-cellular organisation. Shuttling of proteins between compartments is a key mechanism of regulating many processes, including the transcription of DNA in the nucleus [1-3]. Transcription factors and transcriptional regulators are examples of proteins regulated by compartmentalisation and their nuclear accumulation is often restricted in absence of activating signals, either by cytoplasmic tethering or constitutive nuclear export [2]. Mechanistically, members of the karyopherin family recognize specific signals on cargo proteins (larger than 40KDa), namely nuclear localization signals (NLS) and nuclear export signals (NES), and mediate their transition across the nuclear pore complex (NPC), while loading and unloading of cargoes are controlled by the GTPase Ran [1, 3], thus representing an energetic barrier to NC shuttling. Importantly, the function of many transcription factors and regulators is the integration of several signaling inputs. The specificity of the response is dictated by the modulation of frequency, intensity and duration of nuclear-cytoplasmic (NC) shuttling rather than linear nuclear accumulation [4-8]. This change in our understanding highlights the importance of live, non-destructive techniques.

YAP1 and TAZ transcriptional regulators are a perfect example of such complexity. They serve as a hub for a wide range of stimuli, including biochemical (Hippo, [9]) and metabolic pathways [10, 11], mechanical inputs (rigidity, shape, stiffness, cell density and shear stress) [12-19], polarity and other signalling cascades (GPCRs, Akt, JNK) [13, 20, 21]. YAP1 and TAZ are master regulators of cell proliferation, apoptosis, phenotypic plasticity [22, 23] and unsurprisingly they are involved in all the steps of tumorigenesis [24]. In the canonical view of the pathway, YAP1 and TAZ activity is inhibited by nuclear exclusion upon LATS1/2 (the main kinases of Hippo pathway downstream of MST1/2) phosphorylation on key serine residues, and subsequent binding to 14-3-3 proteins or proteasomal degradation. When the phosphorylation is low, YAP1 and TAZ can accumulate into the nucleus and bind to their DNA-binding partners TEAD1-4, BRD4 and MED1, which also contribute to their nuclear accumulation. However, this over simplistic model has been challenged by recent findings that LATS-phosphorylated-YAP1 can be found in the nucleus and that nuclear accumulation is not sufficient for YAP1-driven transcriptional activity [12, 25]. Moreover, several LATS-independent mechanisms have been shown to affect YAP1 and TAZ NC shuttling and activity, such as nuclear deformation [19], cell cycle [26], Src family kinases [13, 25, 27-29] and, more recently, phase separation [30, 31]. Despite the intense studies on these transcription regulators during the years, there is no consensus on how their NC shuttling is regulated.

Historically NC shuttling has been investigated with static methods, on fixed cells or subcellular fractions, with low temporal and spatial resolution, and using chemical such as the export inhibitor Leptomycin B. More recently, measurement of protein shuttling has been revolutionised by the use of fluorescent dyes and proteins [3, 32]. Without perturbation, the partitioning of fluorescent signal between compartment reflects the equilibrium position of the various shuttling process influencing the fluorescently tagged protein. The application of light-driven perturbations, such as photobleaching, provides more information about rates of transit between compartments. However, one downside of photobleaching is that it is inherently destructive by irreversibly

damaging the fluorophore, which limits the researcher's ability to make repeated measurements and typically generates only a single intensity decay curve, which limits the mathematical fitting to derive shuttling rates.

During the last decade, several optogenetic systems have been developed to control NC localisation of proteins within a few seconds upon light illumination. Early examples of light-mediated NC shuttling [33, 34] led to irreversible nuclear accumulation and they have been surpassed by reversible methods based on light-sensitive proteins. The common idea underlying optogenetic systems is the light-dependent conformational change of photoreceptors fused with the proteins of interest, that can be exploited to manipulate a wide range of cellular processes [35]. Desired protein localization upon light illumination has been achieved with two strategies so far: two-components systems, in which a bait protein is anchored to one compartment and the interaction with the prey protein is light-dependent [36-39], and one-component systems, in which NES/NLS peptides are caged/exposed upon light illumination [40-43]. Interestingly, the former strategy has been recently used to develop light-induced control of cellular forces and, as a consequence, of YAP1 localisation [44]. In this work, we exploited an optogenetic tool, namely LOV-TRAP [45, 46], for studying NC shuttling based upon light-induced release and sequestration of POI. We present detailed methods for the molecular biology, imaging, and analysis of this tool. Furthermore, the utility of the method is demonstrated by measuring the nuclear import and export rates of mCherry, YAP1, YAP1 mutants, and TAZ. We show that import and export rates, despite the wide intercellular variability, are correlated within the same cell, and that the export rate is the main determinant of wild-type YAP1 distribution. Finally, we provide the proof of principle that multiple proteins can be recorded simultaneously within the same cell by analysing YAP1 and TAZ nuclear transit rates.

Results

To establish an optogenetic system for protein shuttling studies, we adapted the LOV-TRAP system [45, 46]. With this tool, a mitochondria-tethered LOV domain interacts with its binding partner Zdk98 (Zdk hereafter), fused to the POI labelled with a fluorescent marker. Upon blue-light illumination, LOV and Zdk dissociate, releasing the POI into the cytoplasm within a fraction of a second and enabling subsequent monitoring. We selected the outer surface of mitochondria for sequestration because their distinctive and discrete morphology is well suited to image segmentation. Furthermore, the outer membrane is directly in contact with a large area of the cytoplasm. Therefore, we fused the LOV domain to the mitochondrial anchor sequence TOM20, while the POI was fused to a Zdk peptide sequence. The fluorophore mCherry was selected to visualise the target protein because it is excited with sufficiently long wavelength light to exclude the possibility of triggering a conformational change in the LOV domain. Fig. 1A and Fig. S1A shows a schematic diagram of the constructs and their expected localisation, and expected response to blue light inducing a conformational change in the LOV domain.

An opto-release system for studying nuclear cytoplasmic shuttling

We began by testing if a fusion of the Zdk peptide to mCherry was capable of localising the fluorescent protein to mitochondria in the presence of the TOM20-LOV protein. Cells expressing histone H2B-mTurquoise fusion were co-transfected with these constructs and additionally labelled with a MitoTracker™ dye to allow visualisation of the different compartments. Fig. 1B shows that this approach labels the nucleus and mitochondria in the expected way. Importantly, Zdk-mCherry exhibited expected enrichment to mitochondria in the presence of the TOM20-LOV fusion (Fig. 1B and Fig. S1B, where we show localisation without sequestration). All the constructs used in this study have expected localisation, size and transcriptional activity without sequestration, confirming that these parameters were not affected by fusion with Zdk and mCherry (Fig. S1C-E). We next investigated the effect of 458 nm light illumination. Fig. 1B shows that blue light illumination led to reduced mitochondrial localisation and increased Zdk-mCherry in both the cytoplasm and nucleus. Upon cessation of illumination, the Zdk-mCherry fusion exhibited a progressive transition back to the mitochondria. Quantification of the fluorescent signal in mitochondrial, cytoplasmic, and nuclear compartments confirmed the release and re-binding of Zdk-mCherry to the mitochondria, illustrated in Fig. 1C. Of note, the rate of fluorescence increase and decrease in the nucleus was much slower than that in the cytoplasm. This is most likely related to the rate of nuclear entry and exit of Zdk-mCherry being slower that the kinetics of release and re-binding of the Zdk peptide to the LOV domain. We reasoned that this difference could be exploited to gain quantitative information about the rates of nuclear import and export of proteins. To this end, we developed a computational tool for automatically segmenting the mitochondria, nuclear, and peri-nuclear cytoplasm excluding mitochondria. The time series data generated for each compartment (Fig. 1C) was then fitted to a series of ordinary differential equations (ODEs) (Fig. 1D), with a workflow demonstrated in Fig. 1E.

Supervised semi-automated segmentation of cellular compartments using a Graphical User Interface

To accurately extract quantitative information about the localisation of the fluorescent Zdk-fusion, we developed a supervised Graphical User Interface (GUI) in MATLAB for thresholding the different cellular compartments. Upon loading the imaging data (Fig. S2A), the region containing the cell of interest can be selected. The appropriate threshold for identifying the whole cell is then

set using a sliding tool that provides a real-time image of the result of the thresholding (Fig. S2B). Once an appropriate value has been selected, the process is repeated for the thresholding of the mitochondria, and then the nucleus (Fig. S2C). In the analysis presented here, nuclear segmentation was based on the fluorescent histone image and mitochondrial segmentation was based on MitoTracker™. Thresholding of the cytoplasmic compartment was used to define a region around the nucleus, with mitochondrial regions automatically excluded. We typically chose a threshold that excluded thinner parts of the cell periphery that did not fill the whole z-plane being acquired. Once thresholds are set, the GUI generates both visual plots and a numerical data file with the rates of binding and unbinding of the fluorescent Zdk fusion protein from mitochondria and its rates of nuclear entry and exit (Fig. S2C). We added an additional feature to account for possible changes in the intensity of fluorescent cellular, nuclear, and mitochondrial labels during the imaging. This involved allowing for the thresholding parameters to be re-defined at varying points during the time series. The result of this dynamic thresholding could then be compared with constant threshold values, with the method giving smaller errors in fitting selected for subsequent quantitative analysis.

Differential equations to model nuclear import and export

Having generated numerical data of the localisation of Zdk-fusion protein of interest over time, we then sought to determine the rates of nuclear entry and exit. We used ODEs to model this as a system with three key variables: the amount of Zdk-fusion bound to mitochondria, the amount in the cytoplasm, and the amount in the nucleus (Fig. 1D). Transitions were permitted from the mitochondria to the cytoplasm, and vice-versa, and from the cytoplasm to the nucleus, and vice-versa. The rate of transition on and off mitochondria and rates from cytoplasm to nucleus and nucleus to cytoplasm transfer were fitted simultaneously from the system of ODEs. To account for any photobleaching, we applied a normalisation method to ensure that the total level of fluorescence was constant over time. This improved the data fitting.

Fig. 1F,G show the directly measured mitochondrial release and re-binding rates and the inferred rates of Zdk-mCherry nuclear entry and exit. As we expected, the rates of transit on and off the mitochondria were considerably faster than the nuclear transit rates (compare Fig. 1F with “Optorelease” samples in Fig. 1G). Our methodology uses information from both the release and re-binding phases of the experiment to determine the nuclear entry and exit rates. Fig. S3A,B shows the advantage that this confers over using only the release or only the re-binding phase, with two-fold and eight-fold reductions in the intervals of plausible fitted parameter values when both release and re-binding phases are used compared to release and re-binding phases, respectively. We sought to corroborate the rates of nuclear entry and exit using a conventional fluorescence loss in photobleaching method (FLIP). In this method, we continuously deplete the Zdk-fluorescence at a location either in the cytoplasm (cytoFLIP) or the nucleus (nucFLIP) and record the diffusion of bleached fluorophore in the other compartment. Fig. 1G shows good concordance between the rates measured using our opto-release method and cytoFLIP. Of note, if we performed nucFLIP with continuous bleaching at a point in the nucleus, then the rates of nuclear entry and exit diverged from those measured using both cytoFLIP and opto-release. More specifically, the inferred rates were faster. This is most probably due to direct photobleaching of the fluorophore in the cytoplasm above and below the nucleus. This highlights an important caveat of FLIP experiments – namely the choice of photobleaching location.

Application of opto-release methodology to YAP1 and TAZ

Having established that our method involving light-dependent release of a molecule from sequestration on the outer surface of mitochondria was capable of measuring nuclear entry and exit rates, we applied our method to measure the nuclear import and export rates of the transcriptional regulators YAP1 and TAZ. YAP1 and TAZ were fused to the Zdk peptide and mCherry. Fig. S1E confirms that these chimeric proteins retained their expected ability to drive transcription from a TEAD-dependent promoter, indicating that fusion with fluorophore and Zdk peptide didn't affect binding to other proteins. As before, blue light was used to release YAP1 and TAZ from sequestration and their redistribution into the cytoplasm and nucleus was tracked. After 600 seconds, the blue light illumination was stopped and the return of signal to the mitochondria was monitored (Fig. 2A). The GUI interface described above was then used to extract quantitation (Fig. 2B,C) that was then fitted to the model (Fig. 2D-H). These analyses reveal that both YAP1 and TAZ have slightly lower mitochondria release/recovery rates (Fig. 2D-F), but elevated nuclear import and export rates compared to mCherry, with TAZ rates being slightly faster than the rates of transit across the nuclear envelope for YAP1 (Fig. 2G,H). Once again, we confirmed that measurements obtained by optogenetic release and re-sequestration of YAP1 agreed with data obtained using more conventional FLIP methodology (Fig. S4A-I).

Active YAP1 is subject to reduced rates of nuclear export

Compartmentalization of YAP1 and TAZ is regulated by different post-translational modifications and, despite recent evidences on the importance of methylation and acetylation, the most characterised is phosphorylation. YAP1 and TAZ are negatively regulated by LATS1/2-dependent phosphorylations, downstream of the Hippo pathway, and conversion of these residues to alanine generates a LATS1/2-insensitive YAP1_5SA mutant that shows nuclear localisation and higher transcriptional activity. On the contrary, the YAP1_S94A mutant is transcriptionally inactive and accumulates in the cytoplasm, due to its inability to bind the transcriptional cofactor and nuclear tether TEAD. We investigated if YAP1_5SA and YAP1_S94A mutants exhibited different nuclear import and export rates. Fig. 3A-C and Fig. S5A-E show that the most prominent effect of 5SA mutations is reduced nuclear export compared to the wild-type isoform. In contrast, this doesn't hold true for the YAP1_S94A mutant, that shows rates comparable to the wild-type isoform. Rates of nuclear import and export are consistently correlated as shown for YAP1 and its mutants in Fig. 3D. Cells with high rates of YAP1 nuclear import also had high rates of nuclear export. These data suggest that the energetic cost of transit across the nuclear pore might be highly variable between cells, but that this variation in cost applies to both nuclear entry and exit. Furthermore, even though there is considerable inter-cellular variation in the rates, the process remains subject to regulation. These results support our previous findings that YAP1_5SA nuclear persistence can be explained by slower nuclear exit, while cytoplasmic enrichment of S94A at steady state cannot simply explained by regulation of NC shuttling and thus requires additional explanations, such as tethering by cytoplasmic proteins [25].

Import and export rates are correlated

We were intrigued that the variance in import and export rates spanned an order of magnitude and investigated if this variation might correlate with differences in cell or nuclear morphology, as has been suggested for nuclear import previously [19]. Fig. 4A-E shows correlation analysis of import and export rates with a range of nuclear morphology parameters. Some correlations are

entirely trivial, such as the positive association between area and perimeter, whereas as others are more intriguing, for example, the ratio of import and export rates was strongly correlated with the relative NC distribution. This latter metric reflects the relative segregation of any molecules that were not effectively sequestered by the LOV domain prior to the period of illumination. This is reassuring because in a simple model the ratio between relative rates of import and export should reflect the distribution of molecules between the two compartments at steady state. However, it is not possible to attach too much significance to this as the initial nuclear and cytoplasmic distributions of the fluorophore are assumed to be linearly proportional to the fitted compartment transfer rates and initial mitochondrial intensity in the model fitting. Thus, this observation reflects that our modelling approach is internally consistent. That said, import/export ratio positively correlates with NC distribution for all the proteins analysed, whereas single values of import and export did not, suggesting a biological information beyond the mere technical control. Similarly, import/export ratio positively correlates with nuclear area to cytoplasmic area ratio. Since fitting population intensities, this might reflect that larger nuclei will contain relatively greater levels of fluorescent molecules. Interestingly, the cytoplasmic shape parameters did not show any significant correlations with import and export rates (Fig. S6A-E). More intriguingly, we note that only in the case of YAP1 there was a negative correlation between the export rate and nuclear/cytoplasmic ratio and nuclear area/cytoplasmic area (Fig. 4F). This suggests that tuning of the export rate is the main determinant of the overall nuclear/cytoplasmic distribution of YAP1 and that it becomes reduced as the nucleus takes up a larger area of the cell. Plots relating nuclear import to the same parameters did not show any correlation. The lack of correlation between export rate of mCherry, TAZ, or the YAP1 mutants, with nuclear/cytoplasm ratio or nuclear area/cytoplasmic area indicates that this regulation is specific to wild-type YAP1 and that some mechanisms don't apply to YAP1 mutants (such as cytoskeletal regulation of YAP1_5SA mutant [25].

Simultaneous measurement of YAP1 and TAZ nuclear transit rates reveals that they are correlated

The observation of variance in nuclear transit rates between cells prompted us to wonder if the transit rates of two different proteins in the same cell might be correlated. Testing this idea using conventional FLIP methodology would be highly challenging as it would require both bleaching and imaging two fluorophores simultaneously, with significant potential for unintended bleaching artefacts. However, using the opto-release system with two differently labelled POIs would have fewer problems. Therefore, we labelled YAP1 with Venus and TAZ with mCherry and confirmed that proteins could be tracked in parallel (Fig. 5A). Fig. 5B,C and Fig. S7A-C show that mitochondrial release and nuclear import are similar between YAP1 and TAZ, but the latter shows increased nuclear export (Fig. 5C). This suggests a lower tethering of TAZ in the nucleus compared to YAP1, maybe due to the relative contribution of different mechanisms, such as YAP1 regulation by the cytoskeleton [13, 16] and the presence of different NLS and NES sequences in YAP1 and TAZ [47, 48]. Importantly, both export and import rates of YAP1 significantly correlate with those of TAZ, indicating still a large overlap between the mechanisms regulating NC shuttling of the two proteins (Fig. 5D,E).

Discussion

Decoding the complex regulatory inputs governing the NC distribution of proteins requires accurate measurement of rates of nuclear entry and exit. During the last decade, several works showed that on YAP1 and TAZ converge an incredibly large number of different signals, from cellular architecture and microenvironment geometry to metabolic and biochemical pathways [49]. Here, we implement an optogenetic system to track the NC shuttling of fluorescent YAP1 and TAZ proteins coupled to mathematical modeling to derive nuclear import/export rates. This system builds upon the previously reported LOV-TRAP optogenetic tool that allows protein dissociation within a fraction of a second upon illumination with blue light (450-490 nm). In our system, which we term 'opto-release', we exploited the light-induced dissociation of the LOV domain tethered on mitochondria surface from a previously identified synthetic peptide (Zdk) fused to YAP1 or TAZ and then monitor their sub-cellular distribution over time. With this system we can rapidly generate a pool of fluorescently labeled cytoplasmic YAP1 and TAZ that can be tracked in the cell after release from mitochondria (light) and recovery (dark). The LOV-TRAP system has several advantages over other optogenetic systems for this purpose: i) Zdk is a small peptide and doesn't interfere with endogenous activity of YAP1 and TAZ (as shown in Fig. S1E); ii) the LOV domain utilizes an endogenous chromophore (flavin mononucleotide), reducing external intervention during analysis; iii) it allows the study of multiple fluorescently-labeled proteins with sufficient spectral separation, such as mCherry and Venus (Fig. 5); and iv) it allows rapid, reversible and non-destructive analysis compared to FLIP, thus allowing repeated cycles of light-dark and generation of three curves, from release and recovery dynamics leading to more precise measurements.

Using our opto-release system, we measure YAP1 and TAZ shuttling rates. Despite being larger than mCherry, both YAP1 and TAZ shuttle in and out of the nucleus faster, with roughly 10% of TAZ entering or exiting the nucleus every second. This indicates active mechanisms of both import and export. The rate of YAP1 transit that we measure in epithelial HaCaT cells is similar to that which we previously reported for YAP1 in fibroblasts using FRAP and FLIP methodology [25]. Direct comparison of opto-release with FLIP methods in HaCaT cells showed good concordance when the photobleaching was performed in the cytoplasm. The discordant results of nuclear photobleaching are probably due to direct photobleaching of fluorophore in the cytoplasmic regions of the cell directly above and below the nucleus. The greater height and more cuboidal nature of epithelial cells, such as HaCaT, compared to fibroblasts mean that there will be more cytoplasm above and below the nucleus. This will lead to greater levels of photobleaching occurring directly in the cytoplasm during nuclear FLIP experiments and will confound the results.

In our analysis, mutation of LATS phosphorylation target sites on YAP1 leads to reduced nuclear export that can explain YAP1_5SA nuclear accumulation (Fig. 3B), which is consistent with LATS-mediated phosphorylation being required for effective export [25]. Intriguingly, the YAP1_S94A mutant, which is unable to bind TEAD, is localized in the cytoplasm at steady-state, and in our analysis its import/export rates are close to those calculated for YAP1_WT (Fig. 3A,B) even though it is more cytoplasmic than the wild-type YAP1. This could be explained if there is a pool of YAP1 that remains sequestered in the cytoplasm with binding and unbinding rates that are too slow to measure in the few minutes duration of our assays. Indeed, several studies have suggested cytoplasmic partners for YAP1 [50-53]. In the future, it will be interesting to perform longer release phase experiments with a view to the released YAP1 reaching equilibrium distribution in all sub-cellular compartments. Although we focused exclusively on NC distribution in our study, the opto-release system could equally be applied to problems involving the segregation of proteins between different cytoplasmic compartments: for example, the plasma membrane and cytoplasm. The mathematical modelling of spatial information in addition to temporal information using partial differential

equations as in Ege et al. [25] will also allow us to separate import and export from motility within each compartment.

Interestingly, we could confirm that import and export rates are correlated within the same cell, but show high intercellular variability, as observed in Drosophila [26]. Our conclusion that nuclear export is the main mechanism for the regulation of YAP wild-type activity differs from evidence in *Drosophila*, where Yorkie is mainly regulated by tuning nuclear import [26]. A possible explanation for this discrepancy is that Yorkie (the *Drosophila* homologue of YAP1), lacks PDZ-binding motif that is required for the nuclear accumulation of YAP1 in mammals [54, 55]. By releasing two proteins simultaneously, we could also show that YAP1 and TAZ import and export rates co-varied indicating that they share some regulatory inputs, with LATS-mediated phosphorylation being an obvious candidate. However, we also found evidence for some specificity in regulation between YAP1 and TAZ. For example, wild-type YAP1 export rate negatively correlates with NC ratio, supporting the idea that the rate of nuclear export may be tuned in response to variation in morphological features of the cell, but this was not true for TAZ. It was also not true for YAP1_5SA, which is at least consistent with our previous finding that cytoskeletal inputs primarily tune the export rate of phosphorylated YAP1. Thus, while YAP1 and TAZ share to some extent mechanisms of NC shuttling, specific regulations are in place, as shown by a recent study on TAZ-specific NES/NLS sequences [47]. Of note, FRAP early experiments with GFP-TAZ showed that TEAD-binding defective TAZ mutants exhibit higher nuclear export [56]. Despite correlation of import/export with several morphological metrics, we couldn't observe a link between NC shuttling and nuclear deformation, as reported in Elosegui-Artola et al. [19]. However, we did not apply any direct or indirect perturbations to the nuclear envelope.

In the present study, we report the use of a reversible optogenetic system based upon the LOV-TRAP system [45, 46]. This methodology allows controlled release of fluorescent proteins that can be tracked over time in the different cell compartments. We generated a GUI for thresholding of different cellular compartments and compensation of cell motion. This tool then extracts numerical values for NC localization that are used by differential equations to generate import/export rates. While we have used this system to gain further insights in YAP1 and TAZ NC shuttling, the modular nature of the constructs will make it easy to adapt to a range of transcription factors and regulators, including SMADs, NF-kB, MRTF, IRFs, and STATs. We anticipate that opto-release systems based on this framework will facilitate the understanding of how diverse inputs regulate the sub-cellular localization of proteins and will be of wide utility to cell biologists.

Figure legends

Figure 1: Opto-release system.
(A) Opto-release system specifications; In the dark, Zdk-tagged protein is tightly sequestered on the mitochondria through the interaction with light sensitive LOV domain. The LOV domain is tethered to the mitochondria through TOM20 protein anchor. Upon blue light illumination, the LOV domain changes conformation and releases Zdk-tagged protein.
(B) Representative image of Zdk-flag-mCh constructs release and recovery from mitochondrial sequestration by TOM20-flag-LOVwt. Experiment with 10 min of blue light illumination (the release phase), followed by 10 min of dark recovery without blue light (the recovery phase). Scale bar is 10μm.
(C) Quantification of intensities corresponding to optogenetic release and recovery experiment performed in HaCaT cells transiently transfected with Zdk-flag-mCherry (n=15 cells). Only the mean of all cells from at least 3 biological replicates is showed for clarity. Intensity has been corrected for bleaching and background signal.
(D) System of ordinary differential equations used to derive the shuttling rates of import, k_{imp}, export, k_{exp}, rate of mitochondrial release, k_{rel}, and rate of mitochondrial recovery, k_{rec} for the nucleus, $n(t)$, cytoplasm, $c(t)$ and mitochondria, $m(t)$ at time t. The function ϕ(t) allows the fitting of the escape of intensity to elsewhere in the cell.
(E) Experimental pipeline. Confocal imaging is followed by semi-automated intensity thresholding and shuttling rate analysis with mathematical modelling.
(F) The numerical values of mitochondrial sequestration rates in steady state (darkness), during release and during recovery phases, compared to nuclear import/export rates for Zdk-flag-mCherry (n=16), Number of cells is given in brackets. Boxplot (10&90 percentile, median) represents at least three independent biological replicates. Mann-Whitney U test.
(G) Zdk-flag-mCherry nuclear import and export rates acquired using nuc/cyto FLIP method compared to the optogenetics method. Boxplot (10&90 percentile, median) represents at least three independent biological replicates. The values of optogenetic-derived import/export rates from G are replotted here for clarity and comparison to FLIP. Mann-Whitney U test.

Figure 2: Rates of YAP1 and TAZ nucleocytoplasmic shuttling in HaCaT epithelial cell line.
(A) Representative pictures of Zdk-flag-mCh-YAP1_WT/TAZ constructs release and recovery from mitochondrial sequestration by TOM20-flag-LOVwt. Experiment with 10 min of blue light illumination (the release phase), followed by 10 min of dark recovery without blue light (the recovery phase). Scale bar is 10μm.
(B)(C) Quantification of absolute intensities corresponding to optogenetic release and recovery experiment performed in HaCaT cells transiently transfected with (B) Zdk-flag-mCh-YAP1_WT (n=24) or (C) Zdk-flag-mCh-TAZ (n=22). Only the mean of all cells from at least 3 biological replicates is showed for clarity. Intensity has been corrected for bleaching and background signal.
(D)(E)(F) The numerical values of mitochondrial sequestration rates for Zdk-flag-mCherry-YAP1_WT (n=28) and Zdk-flag-mCh-TAZ (n=22) in steady state (darkness), during release and during recovery phases. Number of cells per each condition is given in brackets. Boxplot (10&90 percentile, median) represents at least three independent biological replicates. Mann-Whitney U test.
(G)(H) YAP1 and TAZ nuclear import and export rates. Boxplot (10&90 percentile, median) represents at least three independent biological replicates. Mann-Whitney U test.

Figure 3: Rates of YAP1 mutants nucleocytoplasmic shuttling in epithelial cell line.
(A)(B) YAP1 mutants nuclear import and export rates. Boxplot (10&90 percentile, median) represents at least three independent biological replicates. Mann-Whitney U test.

(C) Scatterplot of import versus export and line of the best fit for Zdk-flag-mCherry-YAP1_WT (teal), Zdk-flag-mCherry-YAP1_5SA (dark blue), Zdk-flag-mCherry-YAP1_S94A (orange).

Figure 4: Nuclear morphology correlation with import and export.
(A)(B)(C)(D)(E) Import and export correlations with nuclear morphology, specified by area, perimeter, circularity and eccentricity, as well as nuclear-to-cytoplasmic ratio and nuclear area prop. Plots show Zdk-flag-mCherry (A), Zdk-flag-mCh-YAP1_WT (B), Zdk-flag-mCh-YAP1_5SA (C), Zdk-flag-mCh-YAP1_S94A (D) and Zdk-flag-mCh-TAZ (E). Circle colour reflects Pearson correlation (red positive, blue negative) and circle size the p value of the correlation (large, significant; small, nonsignificant).
(F) Negative correlation between export and NC of YAP1_WT.

Figure 5: Rates of YAP1 and TAZ in the same cell.
(A) Representative pictures of release and recovery experiment in Zdk-flag-Venus-YAP1_WT and Zdk-flag-mCh-TAZ using a two-colour optogenetics setup. Scale bar is 10 µm.
(B)(C) YAP1 and TAZ nuclear import and export rates in the same cell. Boxplot (10&90 percentile, median) represents at least three independent biological replicates. Wilcoxon matched-pairs signed rank test.
(D)(E) Scatterplot of YAP1 versus TAZ import (D) or export (E) rates in the same cell. Pearson coefficient (r) and significance (p-value) are also shown.

Supplementary Figure 1: Related to Figure 1. Localization, expression and function of unsequestered Opto-release constructs.
(A) Schematic of various constructs used for opto-release system.
(B) Representative images of HaCaT cells expressing CMV-driven Zdk constructs (transient transfection). Actin is presented in green, DAPI in magenta and mCherry in greyscale. Scale bar is 50 µm.
(C) Boxplot (10&90, median) of nuclear-to-cytoplasmic ratio (log2 scale) corresponding to three experimental repeats of HaCaT cells transiently transfected with CMV-driven Zdk constructs (n>29cells; n>20 for Taz, 2 experimental repeats). Mann-Whitney U test.
(D) Expression of unsequestered Zdk constructs. Western blot showing expression of Opto-release constructs stably expressed in HaCaT cell line. Empty arrowheads point to Opto-release protein (Zdk-flag-mCh 37.5kDa, Zdk-flag-mCh-YAP1_WT 96kDa, Zdk-flag-mCh- TAZ_WT 85kDa) and filled arrowheads point to endogenous protein (YAP1 70kDa, TAZ 50kDa). An arrow points to a cleavage product. Anti-RFP antibody recognizes mCherry fluorescent protein. [Symbol]-tubulin as loading control (42kDa) is also presented.
(E) Luciferase assay using TEAD-driven reporter (5xMCAT) for YAP1/TAZ activity in HaCaT cells following transient transfection with Zdk constructs driven by CMV promoters. Bars represent mean and ± SEM of three independent experiments, each with 3 technical replicates. Mann-Whitney U test, values above each bar represent comparison to MCH negative control.

Supplementary Figure 2: Related to Figure 1. Image analysis pipelines.
(A) GUI cell outline thresholding interface. **(B)** GUI cellular compartments thresholding interface.
(C) GUI settings interface.

Supplementary Figure 3: Related to Figure 2. Jump plots of release fit, recovery fit or release + recovery fit.
(A)(B) Frequency distributions of import (A) and export (B) values that produce fits with sum of squares of error at most twice that of the global optimum. The dots show the location of optimum fit and suggest release-only fitting underestimates both import and export while recovery-only overestimates import and export. All other parameter values were fixed at their global optimums.

Supplementary Figure 4: Related to Figure 2. Confirmation of shuttling rates using FLIP.
(A)(B)(C) Nuclear FLIP analysis of unsequestered Zdk-mCherry constructs. Quantification of absolute intensities normalized to control cell and background intensity, corresponding to FLIP experiment performed in the nucleus of HaCaT cells transiently transfected with (A) Zdk-flag-mCherry (n=32 cells, 4 biological replicates), (B) Zdk-flag-mCh-TAZ (n=17 cells, 3 biological replicates), (C) Zdk-flag-mCh-YAP1_WT (n=21 cells, 3 biological replicates). Only the mean of all cells is showed for clarity.
(D)(E)(F) Cytoplasmic FLIP analysis of unsequestered Zdk-mCherry constructs. Quantification of absolute intensities normalized to control cell and background intensity, corresponding to FLIP experiment performed in the cytoplasm of HaCaT cells transiently transfected with (A) Zdk-flag-mCherry (n=22 cells, 3 biological replicates), (B) Zdk-flag-mCh-TAZ (n=22 cells, 3 biological replicates), (C) Zdk-flag-mCh-YAP1_WT (n=20 cells, 3 biological replicates). Only the mean of all cells is showed for clarity.
(G)(H) YAP1 and TAZ nuclear import and export rates acquired using FLIP methods. The numerical values of nuclear import (k_{imp}) and export (k_{exp}) rates for Zdk-flag-mCherry, Zdk-flag-mCh-TAZ, Zdk-flag-mCh-YAP1_WT are shown. Boxplot (10&90 percentile, median) represents at least 3 independent biological replicates. Mann-Whitney U test.
(I) Table comparing medians of shuttling rates derived using Opto-release method, FLIP nucleus and FLIP cytoplasm.

Supplementary Figure 5: Related to Figure 3. YAP1 mutants parameters.
(A)(B) Quantification of absolute intensities corresponding to optogenetic release and recovery experiment performed in HaCaT cells transiently transfected with (A) Zdk-flag-mCh-YAP1_5SA (n=24) or (C) Zdk-flag-mCh-YAP1_S94A (n=22). Only the mean of all cells from at least 3 biological replicates is showed for clarity. Intensity has been corrected for bleaching and background signal.
(C)(D)(E) The numerical values of mitochondrial sequestration rates for Zdk-flag-mCherry-YAP1_5SA (n=14) and Zdk-flag-mCherry-YAP1_S94A (n=12) compared to Zdk-flag-mCherry-YAP1_WT reproduced from Figure 2 (n=28), in steady state (darkness), during release and during recovery phases. Number of cells per each condition is given in brackets. Boxplot (10&90 percentile, median) represents at least three independent biological replicates. Mann-Whitney U test.

Supplementary Figure 6: Related to Figure 4. Cytoplasm morphology correlation with import and export.
(A)(B)(C)(D)(E) Import and export correlations with cytoplasmic morphology, specified by area, perimeter, circularity and eccentricity. Plots show Zdk-flag-mCherry (A), Zdk-flag-mCh-YAP1_WT (B), Zdk-flag-mCh-YAP1_5SA (C), Zdk-flag-mCh-YAP1_S94A (D) and Zdk-flag-mCh-TAZ (E). Circle colour reflects Pearson correlation (red positive, blue negative) and circle size the p value of the correlation (large, significant; small, nonsignificant).

Supplementary Figure 7: Related to Figure 5. Rates of YAP1 and TAZ in the same cell.
(A)(B)(C) The numerical values of mitochondrial sequestration rates for Zdk-flag-Venus-YAP1_WT and Zdk-flag-mCherry-TAZ (n=14 cells) compared in the same cell in steady state (darkness), during release and during recovery phases. Number of cells per each condition is given in brackets. Boxplot (10&90 percentile, median) represents at least three independent biological replicates. Wilcoxon matched-pairs signed rank test.

Supplementary Movies

Movie 1: Movie shows the first 60 frames (240 seconds) of the blue light illuminated release phase of Zdk-mCherry and the first 60 frames (240 seconds) of the non-illuminated recovery phase.

Movie 2: Movie shows the first 50 frames (200 seconds) of the blue light illuminated release phase of Zdk-YAP1-mCherry and the first 50 frames (200 seconds) of the non-illuminated recovery phase.

Movie 3: Movie shows the first 50 frames (200 seconds) of the blue light illuminated release phase of Zdk-TAZ-mCherry and the first 50 frames (200 seconds) of the non-illuminated recovery phase.

Materials and methods

Cell lines and cell culture

HaCaT immortal keratinocyte cells were acquired from the Cell Services Facility at the Francis Crick Institute. H2B-mTurquoise2 was introduced to cells using the PiggyBac transposon system, where the plasmid of interest is transfected together with a transposase plasmid PBase, and was described before [25]. Cells expressing the construct were selected using Puromycin. All the other plasmids were introduced transiently. Cells were cultured in DMEM (Gibco) with 10% foetal bovine serum (FBS) (PAA Labs) and 1% penicillin-streptavidin (Pen-Strep, Gibco) at 37°C and 5% CO2. The cells were removed from the cell culture dish with 0.1% trypsin and 0.02% versene (both Life Technologies) after washing with PBS (Phosphate buffered saline, 1.5 mM KH2PO4, 8 mM Na2HPO4, 2.7 mM KCl, 137 mM NaCl, pH 7.4). Trypsin was neutralised by addition of cell culture media containing 10% FBS.

Plasmids

All the plasmids generated for the opto-release system were cloned using the Gibson Assembly System (NEB) by combining pRK5.1 backbone with desired PCR fragments according to the manufacturer's instructions. It is based on a previously published LOV-TRAP [45, 46]. The photo-switchable modified common oat (Avena sativa) light-oxygen-voltage (LOV) 2 domain from Phototropin 1 protein is fused to TOM20 protein fragment, which embeds it in the outer mitochondrial membrane. On the other side of the system there is the YAP1/TAZ protein, which is joined to Zdk, an engineered small protein domain based on the Z domain described previously [45, 46], and fluorescent proteins (mCherry or Venus, both photostable in this system and in the timescale of our experiments. YAP1 corresponds to the human YAP1-2γ isoform, which is 504 amino acids long [57] and the mutants were described before [25]. The five serines mutated for the 5SA mutant correspond to serines 61, 109, 127, 164 and 397 (=381) for the isoform used in this study. The two plasmids used for the luciferase experiments, pGL3-49 and pGL3-5xMCAT-49, a gift from Nic Tapon. The pPB-puro-H2B-mTurquoise2 was generated in the lab [25].

Plasmid name	Colours	Promoter	Use	Source
pRK5.1-TOM20-flag-LOVwt	none	CMV	optogenetics	cloned
pRK5.1-Zdk-flag-mCh	mCherry	CMV	optogenetics	cloned
pRK5.1-Zdk-flag-mCh-YAP1_WT	mCherry	CMV	optogenetics	cloned
pRK5.1-Zdk-flag-mCh-YAP1_5SA	mCherry	CMV	optogenetics	cloned
pRK5.1-Zdk-flag-mCh-YAP1_S94A	mCherry	CMV	optogenetics	cloned
pRK5.1-Zdk-flag-mCh-TAZ	mCherry	CMV	optogenetics	cloned
pRK5.1-Zdk-flag-Venus-YAP1_WT	mCherry	CMV	optogenetics	cloned
pGL3-49	luciferase	N/A	luciferase assay	Tapon lab
pGL3-5xMCAT-49	luciferase	N/A	luciferase assay	Tapon lab
pcDNA3-Clover	Clover	CMV	filler plasmid for luciferase assay	Addgene #40259
pGL4.75 CMV-Renilla	renilla	N/A	luciferase assay	Promega, #E6931

DNA Transfection. For transient transfection with plasmid DNA, cells were transfected with Lipofectamine LTX and Plus reagents combination (# 15338100, Thermofisher) according to the manufacturer's instructions. One day prior to the transfection, cells were seeded 0.5-1x 10_6 cells

for Western blotting and luciferase transfection in a 6 well plate, or 20 000-100 000 for live imaging and immunofluorescence in a 24 well plate. Prior to transfection media was changed to Pen-Strep free. On the day of transfection two tubes were prepared (proportions below for 24 well plate):

Tube 1: 100 µl OptiMEM + 1-2 µg DNA + 2 µl Plus reagent

Tube 2: 100 µl OptiMEM + 4 µl Lipofectamine LTX

The two tubes were mixed and incubated for 5 minutes separately, and then 5 minutes together. The transfection mix was added drop wise to cells and incubated for 4-6 hours at 37 °C. Subsequently, the transfection mix was removed and media with Pen-Strep was added. Performing transfection without Pen-Strep is very important and greatly affects transfection efficiency. If the cells are kept longer than 6 hours in the transfection mix, cell viability can become compromised.

Immunofluorescence. All immunofluorescence experiments were performed on cells seeded on glass in MatTek plates (MatTek Co., Ashland, MA, USA). Cells were fixed in 4% paraformaldehyde, washed with 0.01% Triton X100 PBS and permeabilised by incubation in 0.2 % Triton X100, PBS for 20 minutes at room temperature. Samples were subsequently blocked for 1 hour with 5%BSA, 0.01% Triton X100 PBS before incubation with Phalloidin-Atto633 (Sigma, # 68825-10NMOL) and DAPI (Sigma, # d9542-5mg) in 5%BSA, 0.01% Triton X100 PBS 1 hr at RT. Primary antibody was washed off in 3 washes of 5 minutes with 0.01 % Triton X100, PBS, and then retained in PBS until imaging.

Luciferase assay. Luciferase assays were performed with the dual luciferase assay kit (Promega). Cells were lysed using passive lysis buffer. Lysates were placed into a white 96-well plate (Perkin Elmer) to assess Luciferase and Renilla activities using Envision Multilabel plate reader (Perkin Elmer). To normalize, the measurements of firefly luciferase activities were normalized to the renillla luciferase activities of the same sample.

Western Blot. For protein analysis, cells were lysed with 1 x SDS sample buffer (0.32 M Tris pH 6.8, 10% SDS, 50% glycerol, 3M β-mercaptoethanol, 0.05% bromophenol blue) added directly to wells, and then cells were scraped and collected. Each sample was sonicated and then boiled at 95 °C for 5min before being used for Western blotting. Samples were separated on SDS-PAGE gels (Bio-rad). A pre-stained Dual Colour protein ladder (Bio-rad, #1610374) was run with the samples. The proteins in the gel were transferred to polyvinylidene fluoride (PVDF) membrane (GE Healthcare Life Sciences). The membranes were blocked with 2% milk (Marvel) or 2%BSA in TBST (137 mM NaCl, 2.7 mM KCl, 20 mM Tris HCl, pH 7.4, 0.01% Tween 20) for 1 hour at RT, and then incubated with primary antibody at 4°C overnight in 0.1% milk/BSA TBST. After 3 washes with TBST, membranes were incubated 45 min at RT with HRP-labelled secondary antibody in 0.5% milk TBST (1:50 000, Fisher Scientific). The blot was then developed by rinsing it for 1 minute in Luminata WesternHRP Substrate (Millipore) before being exposed in the ImageQuant600RGB machine (GE Healthcare Life Sciences). The list of antibodies used for Western blotting is outlined below.

Antibody	Species	Source	WB	IF
YAP1 (D8H1X)	rabbit mono IgG	Cell Signalling Technology, #14074	1:1000	1:500
TAZ (V386)	rabbit poly	Cell Signalling Technology, #4883	1:1000	1:200
β-tubulin	mouse mono IgG1	Sigma, #T7816	1:5000	1:1000
RFP (5F8)	rat mono IgG2a	Chromotek, #5F8-100	1:1000	N/A
flag tag	mouse mono IgG1	Sigma, #F1804	1:1000	N/A

Statistical analysis. Statistical analyses were performed using Prism software (GraphPad Software). p values were obtained using Mann-Whitney unpaired t–test or Wilcoxon matched-pairs signed rank test, with significance set at $p < 0.05$. Graphs show symbols describing p values: *, $p < 0.05$; **, $p < 0.01$; ***, $p < 0.001$, ****, $p<0.0001$; ns, not significant.

FLIP imaging. Cells were plated at low confluence and cultured overnight in glass bottom MatTek dishes. Cells were transfected, and 24-48 hrs after DNA transfection imaged. One hour prior to imaging, the medium was changed to Leibovitz L-15 media with 10% serum. The cells were subsequently imaged with a Zeiss LSM880 microscope equipped with an argon laser (Zeiss, Germany) and a 63X objective (Zeiss, alpha-Plan Apochromat 63x/1.46 NA oil korr TIRF). For FLIP experiments, bleaching was performed using the laser at 100% capacity with a wavelength corresponding to fluorophore excitation wavelength at a single square ROI of 8x8 pixels (4.4 mm2). All images were 12-bit and 256x256 pixels. Before photobleaching, 3 measurements of fluorescence were taken. The ROI was then photobleached between every frame for 2 seconds using maximum laser power. A series of 150 images were taken every 2 seconds for up to 5 minutes. For nucFLIP, bleaching region was placed in the nucleus, wile for cytoFLIP – in the cytoplasm.

Optogenetics light activation. Cells were plated at low confluence and cultured overnight in glass bottom MatTek dishes. Cells were transfected, and 24-48 hrs after DNA transfection imaged. One hour prior to imaging, the media was changed to Leibovitz L-15 medium with 10% serum supplemented with MitoTracker Deep Red (10 000x, #M22426) for staining the mitochondria. Half an hour prior to imaging, the medium was changed again to Leibovitz L-15 medium with 10% serum without the stain.

The cells were subsequently imaged with a Zeiss LSM880 microscope equipped with an argon laser (Zeiss, Germany) and a 40X objective (Zeiss, Plan Apochromat 40x/1.3 NA oil korr DIC M27) with an environmental chamber set at 37°C. Optogenetic activation was performed using 458 nm laser line at 1% laser power on the bleaching function with 50 iterations selecting an area encompassing the whole cell. Before activation, 5 frames were imaged without photoactivation/bleaching function. Then, 150 frames of release with photoactivation and 150 frames of recovery without photoactivation were acquired. Frames were acquired approximately 4 sec apart, as this corresponds to the approximate speed of light recovery of AsLOV2 domain [39, 58]. In order to simultaneously acquire two or three other channels, a beam splitter 458/514/561/633 was used, which allows imaging in the cyan, yellow, red and far-red colours compatible with light activation at 458 nm. Nuclei are imaged with very low 458 nm laser power which did not interfere with light activation at the same wavelength. Mitochondria are imaged in the far-red spectrum. The proteins of interest can be placed in the yellow (Venus) or the red (mCherry) channels.

Immunofluorescence quantification for nuclear-to-cytoplasmic ratios. For quantification of subcellular localization of protein of interest, the nuclear-to-cytoplasmic ratio was calculated manually. For each cell, a single region of interest (ROI) square of 8x8 pixels was placed in the nucleus and cytoplasm. ROIs were always selected in the DAPI channel of IF images to avoid bias. The cytoplasmic ROI was then confirmed to be in the correct cell by checking the actin channel. The nuclear ROI was divided by the cytoplasmic ROI to derive nuclear-to-cytoplasmic ratio.

FLIP quantification. For quantification of FLIP (Fluorescent Loss In Photobleaching) experiments, MetaMorph (Molecular Devices) was used to follow the integrated intensities of six different square ROIs of the same size as the bleached ROI: the bleached ROI, two reporting ROIs (one in the same compartment as the bleached point and one in the other compartment), two controls ROIs (one in the nucleus and one in the cytoplasm of one control cell) and one ROI outside any cells to measure the background intensity. The two nuclear ROIs and the cytoplasmic ROI of the bleached cells were positioned to be at approximately equal distances from one another. To normalize, first the background intensity was subtracted from the five other intensities measured in the cells. Then, the intensities measured in the cell of interest (three ROIs) were normalized by dividing by the average intensity of the two control ROIs. These data were plotted in the illustrative graphs.

To extract import and export rates, the nuclear and cytoplasmic compartments were determined manually in MATLAB using the roipoly command (found in the Image Processing toolbox). The total population intensity of each compartment over time was then extracted based on these defined regions. Background subtraction and normalisation to the average of nuclear and cytoplasmic regions in the control cell was then carried out (as above). A simpler differential equation model than that employed in [25] was then fitted to this dynamic intensity data, including only temporal data and not spatial data. We fit to the population intensities using a system of ODEs given by

$$\frac{dn(t)}{dt} = -k_{exp}n(t) - k_{imp}c(t) - \delta_n\left(\eta_1 n(t) + \lambda e^{(-\eta_2 t)}\right) \quad ,$$

$$\frac{dc(t)}{dt} = k_{exp}n(t) - k_{imp}c(t) - \delta_c\left(\eta_1 c(t) + \lambda e^{(-\eta_2 t)}\right),$$

$$\delta_n = \begin{cases} 1, & \text{bleach in nucleus} \\ 0, & \text{else} \end{cases}, \ \delta_c = \begin{cases} 1, & \text{bleach in cytoplasm} \\ 0, & \text{else} \end{cases},$$

where $n(t)$ and $c(t)$ give, respectively, the total nuclear and cytoplasmic intensities at time, t. The parameter k_{exp} gives the export rate from the nucleus to the cytoplasm and k_{imp} the import rate from the cytoplasm to the nucleus. The final functions correspond to intensity decay due to bleaching depending on whether the bleach is in the nucleus or cytoplasm. A single decay parameter η_1 allows the model to fit the bleach reasonably well, but underestimates the rapid initial bleach. Hence a decaying exponential function is also incorporated such that the bleach is effectively modelled by a double exponential, one with a rapid rate and the other a slower rate. This double exponential will clearly estimate the rate of bleaching better than a single exponential could (due to a greater degree of fitting freedom) and allows more robust estimates of population intensity transfer between compartments. The initial conditions are given by $n(0) = n_0$ and $c(0) = c_0$. At steady-state, prior to bleaching,

$$n_0 = k_{imp}/k_{exp}c_0. \quad (1)$$

An analytic solution to the ODEs exists, however we estimated parameters by fitting a numerical solution of the model to the experimental intensity data for each cell. Parameter estimates for k_{exp}, k_{imp}, n_0, c_0, η_1, η_2 and λ were all required. We can reduce the number of parameters to fit by one by taking advantage of the steady-state relationship (1) to fix the initial nuclear intensity in terms of rates and initial cytoplasmic intensity. To optimise parameter fitting, we used the nonlinear model fitting function nlinfit in MATLAB's Statistics and Machine Learning toolbox. Initial guesses for parameters in the nlinfit function were selected by choosing the initial cytoplasmic intensity in the experimental data for c_0 and initial guess of order 10^{-3} based on population intensity analysis carried out in [25] for k_{exp} and k_{imp}. To generate initial guesses for the bleaching decay rates we fitted a double exponential function

$$a(t) = q_1 e^{(-r_1 t)} + q_2 e^{(-r_2 t)}$$

to the total intensity of the entire cell (nucleus and cytoplasm). Initial guesses to this double exponential fit were given as: $[\tilde{q}_1, \tilde{q}_2, \tilde{r}_1, \tilde{r}_2]$=[a(0)/2,a(0)/2,0.5,0.1]. By differentiating this double exponential, $a(t)$, into the form

$$\frac{da(t)}{dt} = -\eta_1 a(t) - \lambda e^{(-\eta_2 t)}$$

the output parameters fitted to the double exponential could be used as initial guesses for η_1, η_2 and λ.

Optogenetic quantification.

Cell Compartment Segmentation GUI.

To extract dynamic intensities of the mitochondria, cytoplasm and nucleus we developed a graphical user interface (GUI) to segment the cellular compartments. Each compartment is segmented by the user selecting appropriate threshold levels in addition to a number of other processing steps. The labelling of the nucleus and mitochondria alongside the GFP labelling of the protein of interest allow temporal segmentation of each compartment. Appropriate compartment threshold levels differ from frame to frame and it would be too time consuming to threshold every compartment for every frame for every cell. In addition, in some frames the signal from a given compartment was too weak to segment independently. Therefore, the segmentation was carried out on median intensity projections of compartment channels. Both a single median intensity projection of the entire movie (single window) and median intensity projections of the movie split into 2, 4 and 8 time windows (multiple windows) were considered. Increasing numbers of time windows leads to greater sensitivity to dynamic compartment movement within the movie but reduces robustness in segmentation.

The GUI is coded in MATLAB, requiring the Image Processing toolbox, and is composed of multiple GUIs that call each other, with each GUI concerning a separate aspect of the image segmentation. The initialising GUI allows the user to determine the file location and channel indices alongside the number of time windows that the movies will be split into for segmentation. The GUI runs the segmentation of compartments firstly for the single window and secondly for the user defined multiple windows. The user zooms in on the cell of interest before manually and

roughly cropping around the cell. They then manually select the desired threshold for segmentation of the cell boundary with the outline of the thresholded cell being overlaid onto the cell image. The maximum intensity of all three channels combined is calculated on a frame by frame basis and the median intensity of all of these frames in the time window of interest used to generate the cell image. The user can select the threshold level using a GUI slider; as the slider moves, the outline of the thresholded cell is updated in real time. Having segmented the cell boundary another GUI pops up and allows the user to segment both the nucleus and mitochondria, making use of median intensity projections of the mitochondrial frames and the 90th percentile intensity projection of the nuclear frames (due to a weaker nuclear signal) in the time window of interest. The boundary of each thresholded compartment is overlaid onto the relevant percentile intensity projection and updated in real time, as the user moves the slider. Plots of the population intensity versus time of the mitochondrial, cytoplasmic and nuclear compartments and total for the entire cell are generated in the same GUI. This allows the user to judge the correct segmentation based not only on the compartment outlines but also on the shape of the intensity profiles over time. If compartments for the single window are currently being segmented then the intensity profiles for all time points are plotted. If compartments for multiple windows are currently being segmented then the intensity profiles corresponding to that time window are plotted, in addition to the intensity profiles of the previously segmented time windows. The intensity profiles of the single window segmentation are also shown. The presentation of current time window intensity profile as well as previous time windows allows the user to judge how well the sections link together, dependent on chosen threshold levels. The presentation of the entire movie's intensity profiles allows comparison between the multiple window and single window approaches in real time. Once all multiple window sections have been segmented, this segmentation is interpolated between time windows. A moving median filter is applied to each compartment frame and the compartment thresholds from each multiple window section interpolated to produce smooth intensity profiles despite having been segmented in independent sections. Both the intensity profile of the single window and multiple windows are saved by the GUI for model fitting.

Background subtraction, bleaching intensity normalisation and non-conserved intensity correction methods

Intensity normalisation consists of three stages: i) background subtraction, ii) normalisation due to bleaching and iii) correcting for escape and return of the protein from the focal plane. The normalisation to account for bleaching should lead to the total intensity being constant over time and this is also what is assumed by the system of ODEs. However, upon release from the mitochondria, the protein of interest does not always remain in the viewing plane and instead escapes elsewhere in the cell. Similarly, during the recovery phase there can be a dramatic inflow of the protein of interest in the viewing plane.

Background subtraction is carried out for each frame. The mean of a 20 pixel by 20 pixel square in the top left hand corner of the movie is calculated over time and subtracted from the compartment intensities.

The intensities are then normalised to account for laser bleaching. The level of laser bleaching is determined from the behaviour of the total intensity of the cell over time, which appears to be nonlinear. The rate of bleaching appears to be composed of two approximately linear phases with gradients being approximately linear in both the release and recovery phases but with differing rates. As such, the total intensity is split into release and recovery phases and a linear fit made to each section. For all time prior to recovery, the bleach is assumed to fit the linear fit to

total intensity in the release phase. From the first point of recovery, bleaching is assumed to fit the linear fit to bleaching of total intensity in the recovery phase.

Since the total intensity is not necessarily conserved due to inflow and outflow from the plane of view, the linear fits in each release and recovery phase are fit to temporal subsections. This avoids fitting a linear model to total intensity profiles that also include rapid outflow or inflow into the viewing plane in addition to low level bleaching. Let C be the median total intensity of the cell over the interval $[0, t_{ss_{end}}]$ where $t_{ss_{end}}$ is the last time-point prior to optorelease. Let t_{rl_1} be the beginning of the release fitting subsection and t_{rl_2} be the end. The linear fit to total intensity between t_{rl_1} and t_{rl_2} is given by $\tilde{y}_{rel} = p_{rel_1} t + \tilde{p}_{rel_2}$ where we impose $p_{rel_1} \leq 0$. Let t_{rc_1} be the beginning of the recovery fitting subsection and t_{rc_2} be the end. The linear total intensity fit between t_{rc_1} and t_{rc_2} is given by $\tilde{y}_{rec} = p_{rec_1} t + \tilde{p}_{rec_2}$ where we impose $p_{rec_1} \leq 0$. To normalise to bleaching over these two phases requires a smooth bilinear fit to the gradual drop in total intensity. In the absence of inflow and outflow from the focal plane, these two linear fits, $\tilde{y}_{rel}$ and $\tilde{y}_{rec}$ should smoothly connect at the end of the release and beginning of the recovery phase ($t = t_{REC_1}$). The linear fit $\tilde{y}_{rel}$ should also smoothly link with the median steady-state intensity, C, at timepoint $t_{ss_{end}}$ and linearly increase beyond this value for $t < t_{ss_{end}}$. However, in cases where the total intensity is not conserved throughout the experiment, we must translate the linear functions $\tilde{y}_{rel}$ and $\tilde{y}_{rec}$ such that $\tilde{y}_{rel}$ smoothly connects with C and $\tilde{y}_{rec}$. We adjust the y-intercept for the release phase according to

$$p_{rel_2} = \begin{cases} \tilde{p}_{rel_2}, & p_{rel_1} t_{ss_{end}} + \tilde{p}_{rel_2} > C \\ C - p_{rel_1} t_{ss_{end}}, & \text{else} \end{cases}$$

and define our translated linear fit as $y_{rel} = p_{rel_1} t + p_{rel_2}$. This links the release fit to the median steady-state intensity. We then adjust the y-intercept of $\tilde{y}_{rec}$ so it lines up with y_{rel} by setting $p_{rec_2} = (p_{rel_1} - p_{rec_1}) t_{REC_1} + p_{rel_2}$. We then define our translated linear fit to the recovery phase as $y_{rec} = p_{rec_1} t + p_{rec_2}$. This gives us a smooth bilinear fit to drop in intensity due to bleaching that is independent of inflow and outflow and fit to differing bleach rates in the release and recovery phases.

Following background subtraction and normalisation of intensity to account for bleaching, we address the issue of non-conserved intensity due to rapid inflow and outflow from the image plane. In some cells, intensity is relatively well conserved. However, in a large number of cases we observe a rapid outflow from the image plane during release and rapid inflow during recovery. In a very small number of cases, we observe rapid inflow to the image plane during release and rapid outflow from the image plane during recovery. Due to the low number of cases of the latter, we only correct for the outflow-inflow case.

To detect cases of rapid outflow in release and rapid inflow in recovery we make use of the initial non-translated linear fits $\tilde{y}_{rel}$ and $\tilde{y}_{rec}$. Firstly, if $\tilde{y}_{rel}(t_{ss_{end}}) < C$ it suggests a discontinuous drop in total intensity upon release. This implies a rapid outflow from the focal plane upon release. Secondly, if $\tilde{y}_{rel}(t_{REC_1}) < \tilde{y}_{rec}(t_{REC_1})$ it suggests discontinuous increase in total intensity upon recovery. This implies a rapid inflow into the focal plane upon recovery. If both of these conditions are satisfied it suggests rapid outflow followed by rapid inflow that we can correct for in the model. If these conditions are satisfied, the narrow time periods of rapid outflow and inflow are identified and the total intensity over these time periods smoothed independently using Lowess. By

considering the intensity profiles and the first derivative profiles, a smooth, monotonically decreasing outflow and smooth monotonically increasing inflow can be generated. A vector of inflow and outflow with the smoothed intensity values over these two time windows and NaNs (not a number) everywhere else is generated.

Mathematical model

As in the FLIP analysis, we fit a system of ODEs to the extracted population intensity data for the mitochondrial, cytoplasmic and nuclear compartments. The ODEs are given by

$$\frac{dm(t)}{dt} = k_{rec}c(t) - K_{rel}m(t) + \phi(t)$$

$$\frac{dc(t)}{dt} = -k_{rec}c(t) + K_{rel}m(t) + k_{exp}n(t) - k_{imp}c(t),$$

$$\frac{dn(t)}{dt} = -k_{exp}n(t) + k_{imp}c(t),$$

where $m(t)$, $c(t)$ and $n(t)$ are the mitochondrial, cytoplasmic and nuclear intensities respectively at time, t. The initial conditions are given by $m(0) = m_0,\ c(0) = c_0$ and $n(0) = n_0$. The rate of export from the nucleus to the cytoplasm and rate of import from the cytoplasm to the nucleus are given by k_{exp} and k_{imp} respectively. The parameter k_{rec} gives the rate at which the protein leaves the cytoplasm and binds to the mitochondria. The parameter K_{rel} gives the rate at which protein leaves the mitochondria and enters the cytoplasmic compartment. The value K_{rel} is dependent on whether the system is in the illumination phase or not i.e.

$$K_{rel} = \begin{cases} k_{rel_{ill}}, & \text{system in illumination phase} \\ k_{rel_{ss}}, & \text{system in steady} - \text{state phase.} \end{cases}$$

The final component of the ODEs is the function, $\phi(t)$, which accounts for cases where the total protein intensity in the system is not conserved in the experimental data, even after normalisation. We shall refer to this further in the model fitting methodology.

Model Fitting

The system of ODEs is fitted to the experimental data using MATLAB's nlinfit function from the Statistics and Machine Learning toolbox. The fitting weights of each compartment are normalised such that each compartment contributes an equal amount to the residuals. Parameters that need fitting in the system are the rates k_{exp}, k_{imp}, k_{rec}, $k_{rel_{ill}}$ and $k_{rel_{ss}}$ and the initial conditions m_0, c_0 and n_0. The model is fit such that the parameter $k_{rel_{ill}}$ is fit only at the release phase and $k_{rel_{ss}}$ only fit at the initial steady-state phase and the recovery phase. The initial conditions need to be fitted since we cannot fix them at their experimental measurements due to noise in the system. We can reduce the number of parameters that need fitting by taking advantage of the steady-state relationships $c_0 = k_{rel_{ss}}/k_{rec}m_0$ and $n_0 = k_{imp}/k_{exp}c_0$ allowing us to fix the initial nuclear and cytoplasmic intensities in terms of other parameters. If the algorithm has identified that total intensity is conserved throughout the experiment then the inflow-outflow function $\phi(t)$ is set to zero everywhere. If the intensity is not conserved then $\phi(t)$ is constructed from the derivative of the inflow-outflow vector (described in the normalisation section) in the sections of smooth, monotonically decreasing release and smooth, monotonically increasing recovery. Everywhere

else, where the inflow-outflow vector is composed of NaNs, the function $\phi(t)$ is set to zero. As initial guesses for our parameters we take $\left[\hat{k}_{rel_{ss}}, \hat{k}_{rel_{ill}}, \hat{k}_{rec}, \hat{k}_{imp}, \hat{k}_{exp}, \hat{m}_0\right] = [0.05, 0.10, 0.05, 0.005, 0.005, \Lambda]$ where Λ gives the median mitochondrial intensity over the first five frames prior to release.

For each cell, the intensity extraction was carried out by splitting each movie into 1, 2, 4 or 8 sections as described in the segmentation section. The system of ODEs was fit to each of these intensity extractions and the mean sum of squares of error for both the entire system and the fit to the nucleus only calculated. The fit with the lowest mean sum of squares of error was selected as being the optimum fit in each case.

Acknowledgements

We thank members of the Crick Advanced Light Microscopy facility for technical support. We are indebted to Hui Wang and Sirio Dupont for thoughtful discussion and advice. A.M.D., R.P.J, M.M., and E.S. were funded by the Francis Crick Institute, which receives its core funding from Cancer Research UK (FC001144), the UK Medical Research Council (FC001144) and the Wellcome Trust (FC001144). M.M. also received funding from Marie Curie Actions—Intra-European Fellowships #625496. K.H. was supported by NIH grant R35GM122596.

Author contributions

A.M.D. performed the experiments, R.P.J. developed the GUI and analytical methods, K.H. provided reagents prior to their publication, M.M. and E.S. conceived the study, A.M.D., M.M., and E.S. wrote the manuscript.

References

1. Fu, X., Liang, C., Li, F., Wang, L., Wu, X., Lu, A., Xiao, G., and Zhang, G. (2018). The Rules and Functions of Nucleocytoplasmic Shuttling Proteins. Int J Mol Sci *19*.
2. Xu, L., and Massague, J. (2004). Nucleocytoplasmic shuttling of signal transducers. Nat Rev Mol Cell Biol *5*, 209-219.
3. Di Ventura, B., and Kuhlman, B. (2016). Go in! Go out! Inducible control of nuclear localization. Curr Opin Chem Biol *34*, 62-71.
4. Hao, N., and O'Shea, E.K. (2011). Signal-dependent dynamics of transcription factor translocation controls gene expression. Nat Struct Mol Biol *19*, 31-39.
5. Purvis, J.E., and Lahav, G. (2013). Encoding and decoding cellular information through signaling dynamics. Cell *152*, 945-956.
6. Gao, Z., Chen, S., Qin, S., and Tang, C. (2018). Network Motifs Capable of Decoding Transcription Factor Dynamics. Sci Rep *8*, 3594.
7. Yosef, N., and Regev, A. (2011). Impulse control: temporal dynamics in gene transcription. Cell *144*, 886-896.
8. Behar, M., and Hoffmann, A. (2010). Understanding the temporal codes of intra-cellular signals. Curr Opin Genet Dev *20*, 684-693.

9. Meng, Z., Moroishi, T., and Guan, K.L. (2016). Mechanisms of Hippo pathway regulation. Genes Dev *30*, 1-17.
10. Sorrentino, G., Ruggeri, N., Specchia, V., Cordenonsi, M., Mano, M., Dupont, S., Manfrin, A., Ingallina, E., Sommaggio, R., Piazza, S., et al. (2014). Metabolic control of YAP and TAZ by the mevalonate pathway. Nat Cell Biol *16*, 357-366.
11. Bertolio, R., Napoletano, F., Mano, M., Maurer-Stroh, S., Fantuz, M., Zannini, A., Bicciato, S., Sorrentino, G., and Del Sal, G. (2019). Sterol regulatory element binding protein 1 couples mechanical cues and lipid metabolism. Nat Commun *10*, 1326.
12. Wada, K., Itoga, K., Okano, T., Yonemura, S., and Sasaki, H. (2011). Hippo pathway regulation by cell morphology and stress fibers. Development *138*, 3907-3914.
13. Calvo, F., Ege, N., Grande-Garcia, A., Hooper, S., Jenkins, R.P., Chaudhry, S.I., Harrington, K., Williamson, P., Moeendarbary, E., Charras, G., et al. (2013). Mechanotransduction and YAP-dependent matrix remodelling is required for the generation and maintenance of cancer-associated fibroblasts. Nat Cell Biol *15*, 637-646.
14. Benham-Pyle, B.W., Pruitt, B.L., and Nelson, W.J. (2015). Cell adhesion. Mechanical strain induces E-cadherin-dependent Yap1 and beta-catenin activation to drive cell cycle entry. Science *348*, 1024-1027.
15. Aragona, M., Panciera, T., Manfrin, A., Giulitti, S., Michielin, F., Elvassore, N., Dupont, S., and Piccolo, S. (2013). A mechanical checkpoint controls multicellular growth through YAP/TAZ regulation by actin-processing factors. Cell *154*, 1047-1059.
16. Dupont, S., Morsut, L., Aragona, M., Enzo, E., Giulitti, S., Cordenonsi, M., Zanconato, F., Le Digabel, J., Forcato, M., Bicciato, S., et al. (2011). Role of YAP/TAZ in mechanotransduction. Nature *474*, 179-183.
17. Chaudhuri, O., Gu, L., Klumpers, D., Darnell, M., Bencherif, S.A., Weaver, J.C., Huebsch, N., Lee, H.P., Lippens, E., Duda, G.N., et al. (2016). Hydrogels with tunable stress relaxation regulate stem cell fate and activity. Nat Mater *15*, 326-334.
18. Nakajima, H., Yamamoto, K., Agarwala, S., Terai, K., Fukui, H., Fukuhara, S., Ando, K., Miyazaki, T., Yokota, Y., Schmelzer, E., et al. (2017). Flow-Dependent Endothelial YAP Regulation Contributes to Vessel Maintenance. Dev Cell *40*, 523-536 e526.
19. Elosegui-Artola, A., Andreu, I., Beedle, A.E.M., Lezamiz, A., Uroz, M., Kosmalska, A.J., Oria, R., Kechagia, J.Z., Rico-Lastres, P., Le Roux, A.L., et al. (2017). Force Triggers YAP Nuclear Entry by Regulating Transport across Nuclear Pores. Cell *171*, 1397-1410 e1314.
20. Codelia, V.A., Sun, G., and Irvine, K.D. (2014). Regulation of YAP by mechanical strain through Jnk and Hippo signaling. Curr Biol *24*, 2012-2017.
21. Basu, S., Totty, N.F., Irwin, M.S., Sudol, M., and Downward, J. (2003). Akt phosphorylates the Yes-associated protein, YAP, to induce interaction with 14-3-3 and attenuation of p73-mediated apoptosis. Mol Cell *11*, 11-23.
22. Zanconato, F., Cordenonsi, M., and Piccolo, S. (2019). YAP and TAZ: a signalling hub of the tumour microenvironment. Nat Rev Cancer *19*, 454-464.
23. Shreberk-Shaked, M., and Oren, M. (2019). New insights into YAP/TAZ nucleo-cytoplasmic shuttling: new cancer therapeutic opportunities? Mol Oncol *13*, 1335-1341.
24. Zanconato, F., Cordenonsi, M., and Piccolo, S. (2016). YAP/TAZ at the Roots of Cancer. Cancer Cell *29*, 783-803.
25. Ege, N., Dowbaj, A.M., Jiang, M., Howell, M., Hooper, S., Foster, C., Jenkins, R.P., and Sahai, E. (2018). Quantitative Analysis Reveals that Actin and Src-Family Kinases Regulate Nuclear YAP1 and Its Export. Cell Syst *6*, 692-708 e613.
26. Manning, S.A., Dent, L.G., Kondo, S., Zhao, Z.W., Plachta, N., and Harvey, K.F. (2018). Dynamic Fluctuations in Subcellular Localization of the Hippo Pathway Effector Yorkie In Vivo. Curr Biol *28*, 1651-1660 e1654.

27. Elbediwy, A., Vincent-Mistiaen, Z.I., Spencer-Dene, B., Stone, R.K., Boeing, S., Wculek, S.K., Cordero, J., Tan, E.H., Ridgway, R., Brunton, V.G., et al. (2016). Integrin signalling regulates YAP and TAZ to control skin homeostasis. Development *143*, 1674-1687.
28. Rosenbluh, J., Nijhawan, D., Cox, A.G., Li, X., Neal, J.T., Schafer, E.J., Zack, T.I., Wang, X., Tsherniak, A., Schinzel, A.C., et al. (2012). beta-Catenin-driven cancers require a YAP1 transcriptional complex for survival and tumorigenesis. Cell *151*, 1457-1473.
29. Tamm, C., Bower, N., and Anneren, C. (2011). Regulation of mouse embryonic stem cell self-renewal by a Yes-YAP-TEAD2 signaling pathway downstream of LIF. J Cell Sci *124*, 1136-1144.
30. Lu, Y., Wu, T., Gutman, O., Lu, H., Zhou, Q., Henis, Y.I., and Luo, K. (2020). Phase separation of TAZ compartmentalizes the transcription machinery to promote gene expression. Nat Cell Biol *22*, 453-464.
31. Cai, D., Feliciano, D., Dong, P., Flores, E., Gruebele, M., Porat-Shliom, N., Sukenik, S., Liu, Z., and Lippincott-Schwartz, J. (2019). Phase separation of YAP reorganizes genome topology for long-term YAP target gene expression. Nat Cell Biol *21*, 1578-1589.
32. Molenaar, C., and Weeks, K.L. (2018). Nucleocytoplasmic shuttling: The ins and outs of quantitative imaging. Clin Exp Pharmacol Physiol *45*, 1087-1094.
33. Engelke, H., Chou, C., Uprety, R., Jess, P., and Deiters, A. (2014). Control of protein function through optochemical translocation. ACS Synth Biol *3*, 731-736.
34. Crefcoeur, R.P., Yin, R., Ulm, R., and Halazonetis, T.D. (2013). Ultraviolet-B-mediated induction of protein-protein interactions in mammalian cells. Nat Commun *4*, 1779.
35. de Mena, L., Rizk, P., and Rincon-Limas, D.E. (2018). Bringing Light to Transcription: The Optogenetics Repertoire. Front Genet *9*, 518.
36. Guntas, G., Hallett, R.A., Zimmerman, S.P., Williams, T., Yumerefendi, H., Bear, J.E., and Kuhlman, B. (2015). Engineering an improved light-induced dimer (iLID) for controlling the localization and activity of signaling proteins. Proc Natl Acad Sci U S A *112*, 112-117.
37. Kennedy, M.J., Hughes, R.M., Peteya, L.A., Schwartz, J.W., Ehlers, M.D., and Tucker, C.L. (2010). Rapid blue-light-mediated induction of protein interactions in living cells. Nat Methods *7*, 973-975.
38. Beyer, H.M., Juillot, S., Herbst, K., Samodelov, S.L., Muller, K., Schamel, W.W., Romer, W., Schafer, E., Nagy, F., Strahle, U., et al. (2015). Red Light-Regulated Reversible Nuclear Localization of Proteins in Mammalian Cells and Zebrafish. ACS Synth Biol *4*, 951-958.
39. Strickland, D., Lin, Y., Wagner, E., Hope, C.M., Zayner, J., Antoniou, C., Sosnick, T.R., Weiss, E.L., and Glotzer, M. (2012). TULIPs: tunable, light-controlled interacting protein tags for cell biology. Nat Methods *9*, 379-384.
40. Niopek, D., Benzinger, D., Roensch, J., Draebing, T., Wehler, P., Eils, R., and Di Ventura, B. (2014). Engineering light-inducible nuclear localization signals for precise spatiotemporal control of protein dynamics in living cells. Nat Commun *5*, 4404.
41. Niopek, D., Wehler, P., Roensch, J., Eils, R., and Di Ventura, B. (2016). Optogenetic control of nuclear protein export. Nat Commun *7*, 10624.
42. Yumerefendi, H., Dickinson, D.J., Wang, H., Zimmerman, S.P., Bear, J.E., Goldstein, B., Hahn, K., and Kuhlman, B. (2015). Control of Protein Activity and Cell Fate Specification via Light-Mediated Nuclear Translocation. PLoS One *10*, e0128443.
43. Yumerefendi, H., Lerner, A.M., Zimmerman, S.P., Hahn, K., Bear, J.E., Strahl, B.D., and Kuhlman, B. (2016). Light-induced nuclear export reveals rapid dynamics of epigenetic modifications. Nat Chem Biol *12*, 399-401.
44. Valon, L., Marin-Llaurado, A., Wyatt, T., Charras, G., and Trepat, X. (2017). Optogenetic control of cellular forces and mechanotransduction. Nat Commun *8*, 14396.
45. Wang, H., and Hahn, K.M. (2016). LOVTRAP: A Versatile Method to Control Protein Function with Light. Curr Protoc Cell Biol *73*, 21 10 21-21 10 14.

46. Wang, H., Vilela, M., Winkler, A., Tarnawski, M., Schlichting, I., Yumerefendi, H., Kuhlman, B., Liu, R., Danuser, G., and Hahn, K.M. (2016). LOVTRAP: an optogenetic system for photoinduced protein dissociation. Nat Methods *13*, 755-758.
47. Kofler, M., Speight, P., Little, D., Di Ciano-Oliveira, C., Szaszi, K., and Kapus, A. (2018). Mediated nuclear import and export of TAZ and the underlying molecular requirements. Nat Commun *9*, 4966.
48. Fang, L., Teng, H., Wang, Y., Liao, G., Weng, L., Li, Y., Wang, X., Jin, J., Jiao, C., Chen, L., et al. (2018). SET1A-Mediated Mono-Methylation at K342 Regulates YAP Activation by Blocking Its Nuclear Export and Promotes Tumorigenesis. Cancer Cell *34*, 103-118 e109.
49. Pocaterra, A., Romani, P., and Dupont, S. (2020). YAP/TAZ functions and their regulation at a glance. J Cell Sci *133*.
50. Kanai, F., Marignani, P.A., Sarbassova, D., Yagi, R., Hall, R.A., Donowitz, M., Hisaminato, A., Fujiwara, T., Ito, Y., Cantley, L.C., et al. (2000). TAZ: a novel transcriptional co-activator regulated by interactions with 14-3-3 and PDZ domain proteins. EMBO J *19*, 6778-6791.
51. Azzolin, L., Panciera, T., Soligo, S., Enzo, E., Bicciato, S., Dupont, S., Bresolin, S., Frasson, C., Basso, G., Guzzardo, V., et al. (2014). YAP/TAZ incorporation in the beta-catenin destruction complex orchestrates the Wnt response. Cell *158*, 157-170.
52. Varelas, X., Miller, B.W., Sopko, R., Song, S., Gregorieff, A., Fellouse, F.A., Sakuma, R., Pawson, T., Hunziker, W., McNeill, H., et al. (2010). The Hippo pathway regulates Wnt/beta-catenin signaling. Dev Cell *18*, 579-591.
53. Zhao, B., Li, L., Tumaneng, K., Wang, C.Y., and Guan, K.L. (2010). A coordinated phosphorylation by Lats and CK1 regulates YAP stability through SCF(beta-TRCP). Genes Dev *24*, 72-85.
54. Wang, S., Lu, Y., Yin, M.X., Wang, C., Wu, W., Li, J., Wu, W., Ge, L., Hu, L., Zhao, Y., et al. (2016). Importin alpha1 Mediates Yorkie Nuclear Import via an N-terminal Non-canonical Nuclear Localization Signal. J Biol Chem *291*, 7926-7937.
55. Oka, T., and Sudol, M. (2009). Nuclear localization and pro-apoptotic signaling of YAP2 require intact PDZ-binding motif. Genes Cells *14*, 607-615.
56. Chan, S.W., Lim, C.J., Loo, L.S., Chong, Y.F., Huang, C., and Hong, W. (2009). TEADs mediate nuclear retention of TAZ to promote oncogenic transformation. J Biol Chem *284*, 14347-14358.
57. Sudol, M. (2013). YAP1 oncogene and its eight isoforms. Oncogene *32*, 3922.
58. Strickland, D., Yao, X., Gawlak, G., Rosen, M.K., Gardner, K.H., and Sosnick, T.R. (2010). Rationally improving LOV domain-based photoswitches. Nat Methods *7*, 623-626.

Figure 1

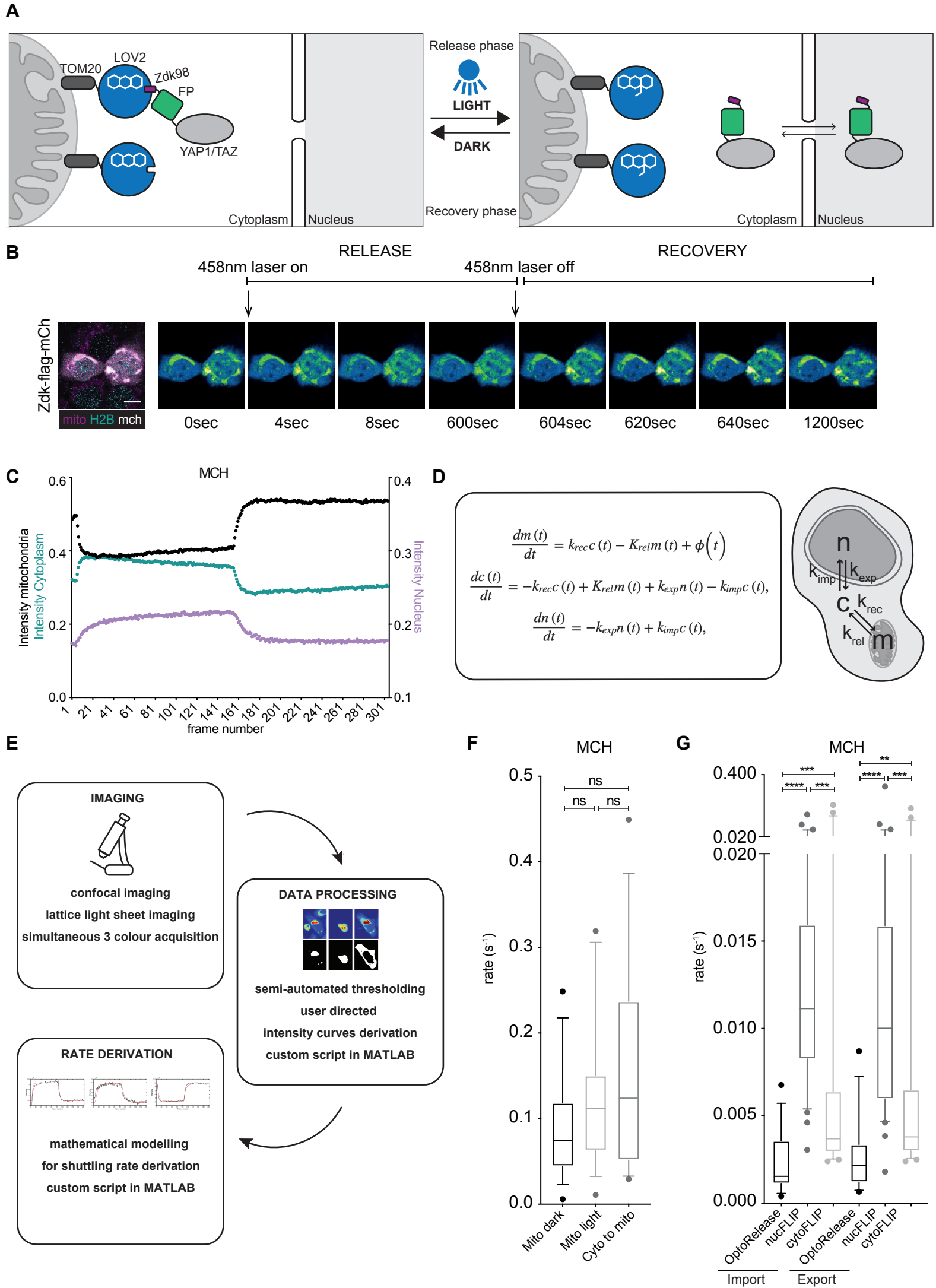
A
TOM20
LOV2
Zdk98
FP
YAP1/TAZ
Cytoplasm
Nucleus
Release phase
LIGHT
DARK
Recovery phase
Cytoplasm
Nucleus
B
RELEASE
RECOVERY
458nm laser on
458nm laser off
Zdk-flag-mCh
mito H2B mch
0sec
4sec
8sec
600sec
604sec
620sec
640sec
1200sec
C
MCH
Intensity mitochondria
Intensity Cytoplasm
Intensity Nucleus
frame number
D
$\frac{dm(t)}{dt} = k_{rec}c(t) - K_{rel}m(t) + \phi(t)$
$\frac{dc(t)}{dt} = -k_{rec}c(t) + K_{rel}m(t) + k_{exp}n(t) - k_{imp}c(t),$
$\frac{dn(t)}{dt} = -k_{exp}n(t) + k_{imp}c(t),$
n
k_{imp}
k_{exp}
c
k_{rec}
k_{rel}
m
E
IMAGING
confocal imaging
lattice light sheet imaging
simultaneous 3 colour acquisition
DATA PROCESSING
semi-automated thresholding
user directed
intensity curves derivation
custom script in MATLAB
RATE DERIVATION
mathematical modelling
for shuttling rate derivation
custom script in MATLAB
F
MCH
rate (s^{-1})
ns
Mito dark
Mito light
Cyto to mito
G
MCH
rate (s^{-1})
OptoRelease
nucFLIP
cytoFLIP
Import
Export

Figure 2

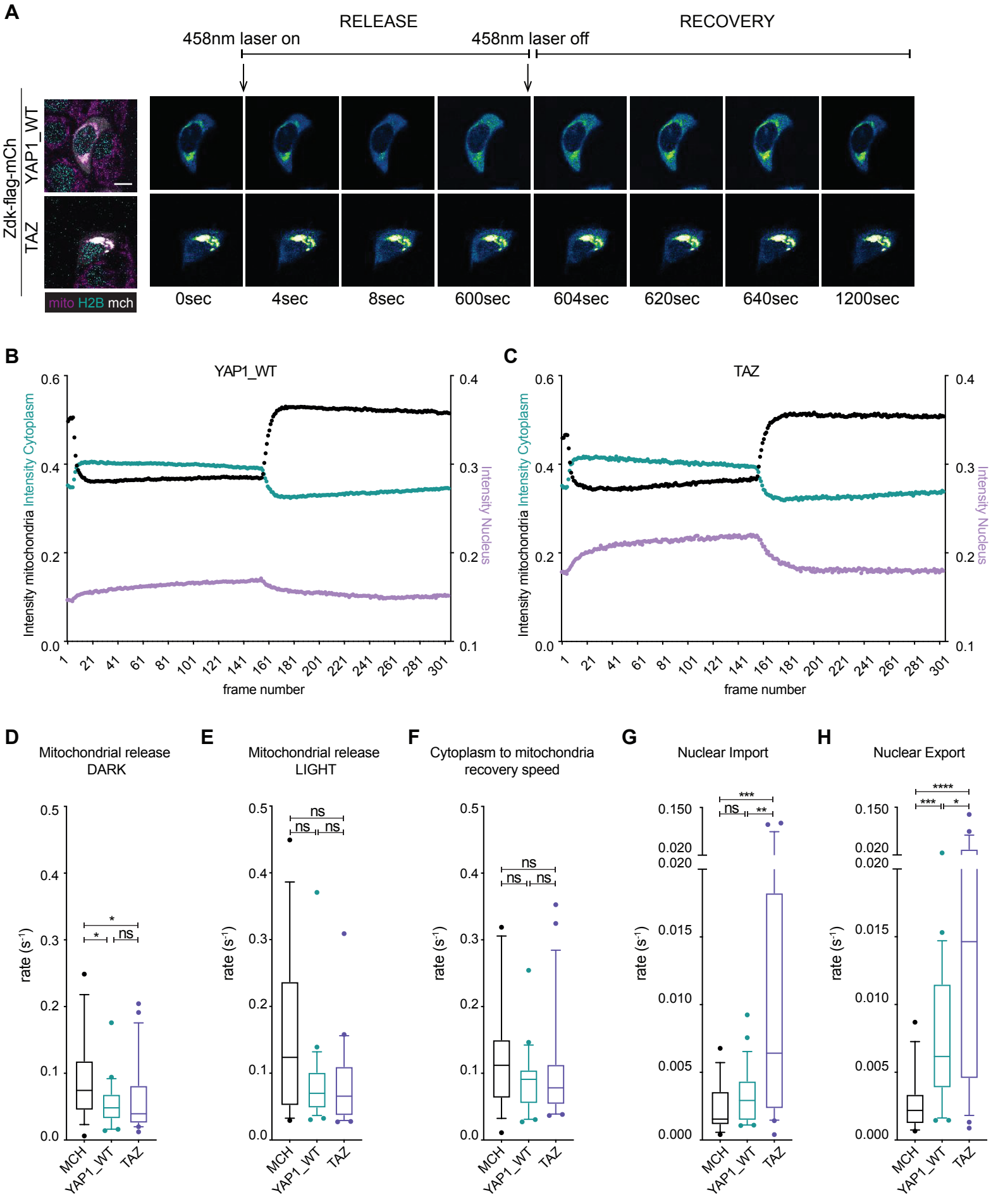
A
RELEASE
458nm laser on
458nm laser off
RECOVERY
Zdk-flag-mCh
YAP1_WT
TAZ
mito H2B mch
0sec
4sec
8sec
600sec
604sec
620sec
640sec
1200sec
B
YAP1_WT
Intensity mitochondria Intensity Cytoplasm
Intensity Nucleus
frame number
C
TAZ
Intensity mitochondria Intensity Cytoplasm
Intensity Nucleus
frame number
D
Mitochondrial release DARK
rate (s-1)
MCH
YAP1_WT
TAZ
E
Mitochondrial release LIGHT
F
Cytoplasm to mitochondria recovery speed
G
Nuclear Import
H
Nuclear Export

Figure 3

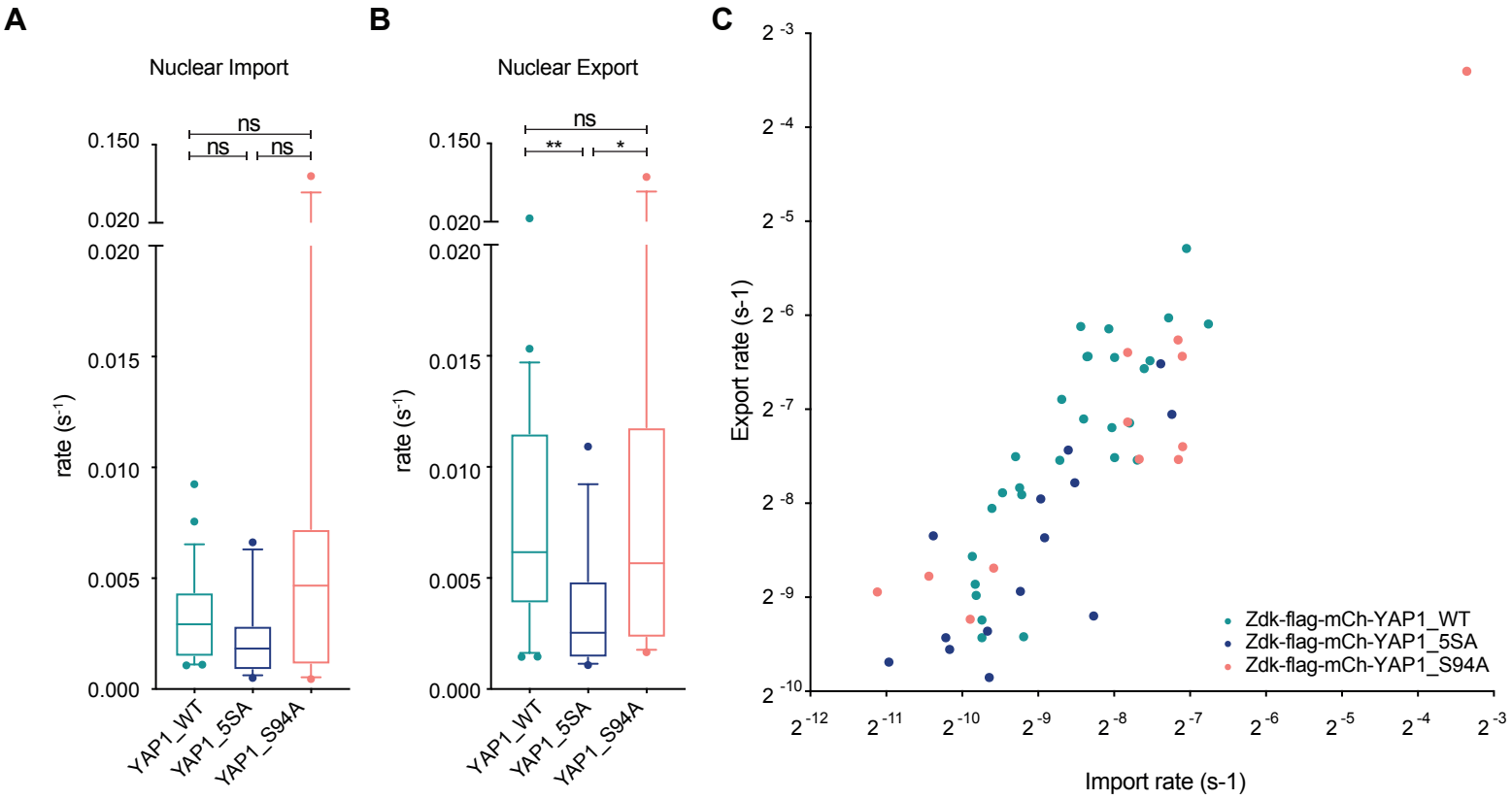
A
Nuclear Import
ns
ns
ns
0.150
0.020
0.020
0.015
0.010
0.005
0.000
rate (s-1)
YAP1_WT
YAP1_5SA
YAP1_S94A
B
Nuclear Export
ns
**
*
0.150
0.020
0.020
0.015
0.010
0.005
0.000
rate (s-1)
YAP1_WT
YAP1_5SA
YAP1_S94A
C
Export rate (s-1)
Import rate (s-1)
Zdk-flag-mCh-YAP1_WT
Zdk-flag-mCh-YAP1_5SA
Zdk-flag-mCh-YAP1_S94A

Figure 4

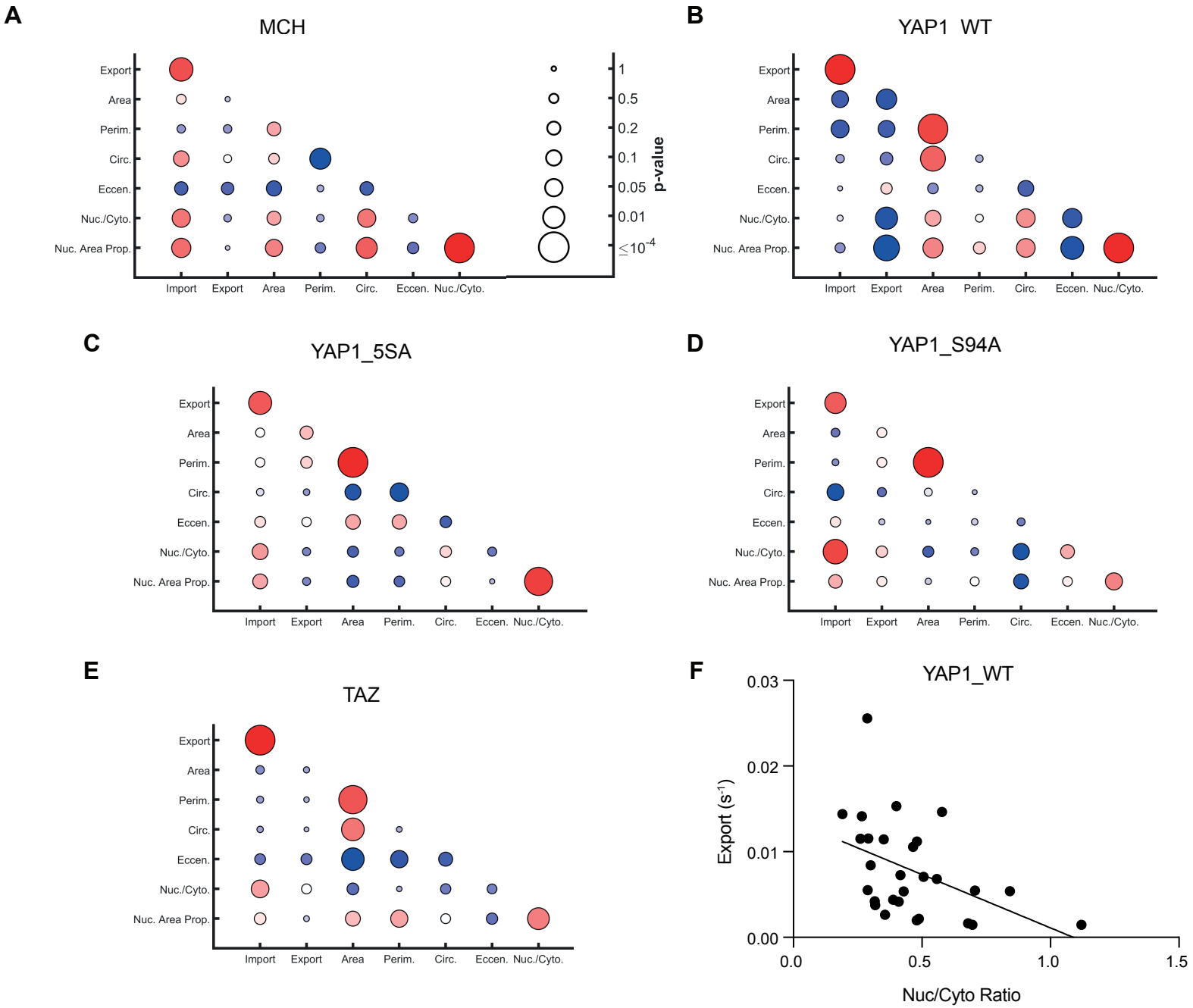
A
MCH
Export
Area
Perim.
Circ.
Eccen.
Nuc./Cyto.
Nuc. Area Prop.
Import
Export
Area
Perim.
Circ.
Eccen.
Nuc./Cyto.
1
0.5
0.2
0.1
0.05
0.01
≤10^-4
p-value
B
YAP1 WT
C
YAP1_5SA
D
YAP1_S94A
E
TAZ
F
YAP1_WT
Export (s^-1)
0.03
0.02
0.01
0.00
0.0
0.5
1.0
1.5
Nuc/Cyto Ratio

Figure 5

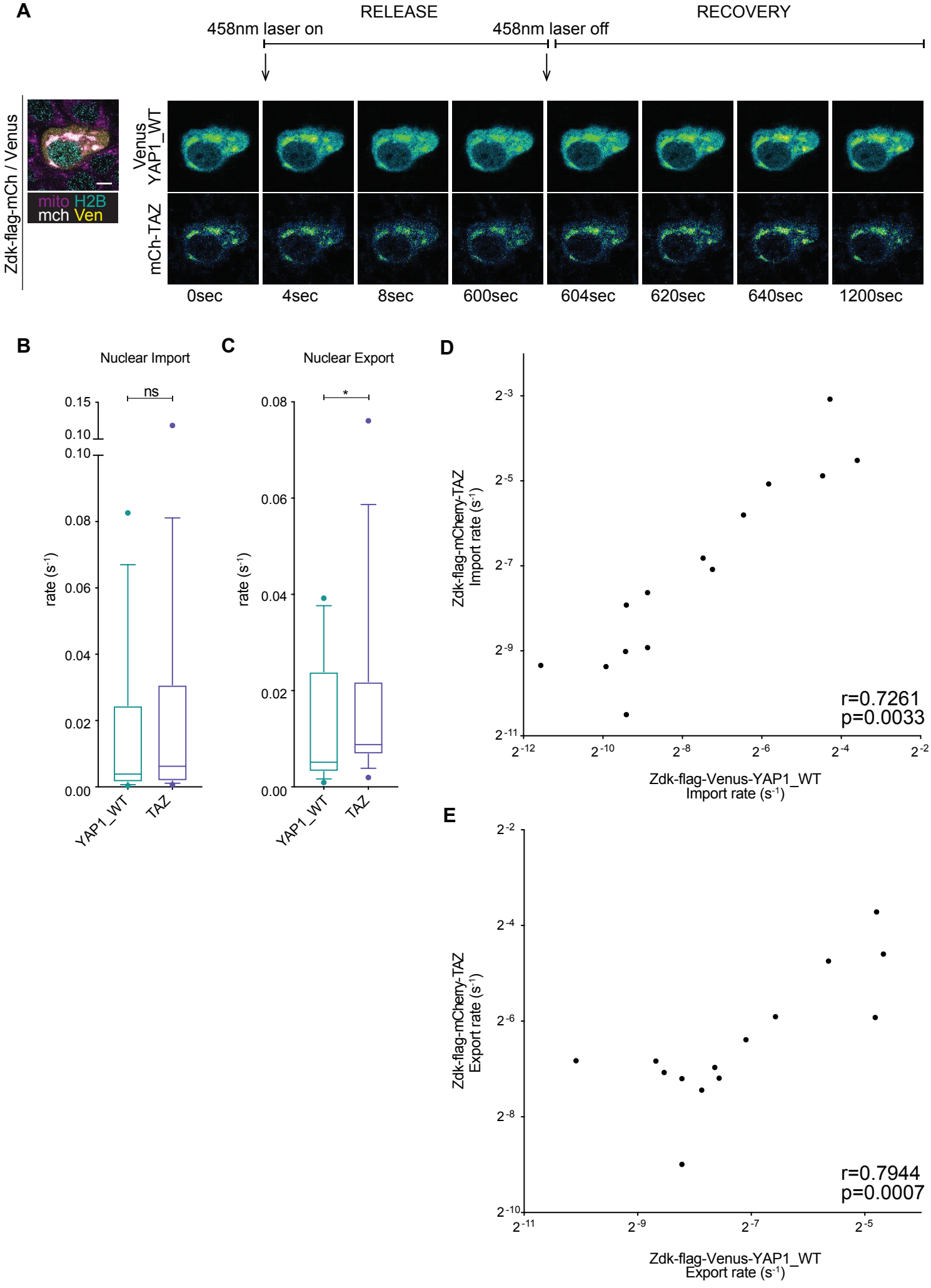
A
RELEASE
RECOVERY
458nm laser on
458nm laser off
Zdk-flag-mCh / Venus
mito H2B
mch Ven
Venus YAP1_WT
mCh-TAZ
0sec
4sec
8sec
600sec
604sec
620sec
640sec
1200sec
B
Nuclear Import
ns
rate (s-1)
YAP1_WT
TAZ
C
Nuclear Export
*
rate (s-1)
YAP1_WT
TAZ
D
Zdk-flag-mCherry-TAZ Import rate (s-1)
Zdk-flag-Venus-YAP1_WT Import rate (s-1)
r=0.7261
p=0.0033
E
Zdk-flag-mCherry-TAZ Export rate (s-1)
Zdk-flag-Venus-YAP1_WT Export rate (s-1)
r=0.7944
p=0.0007

Supplementary Figure 1

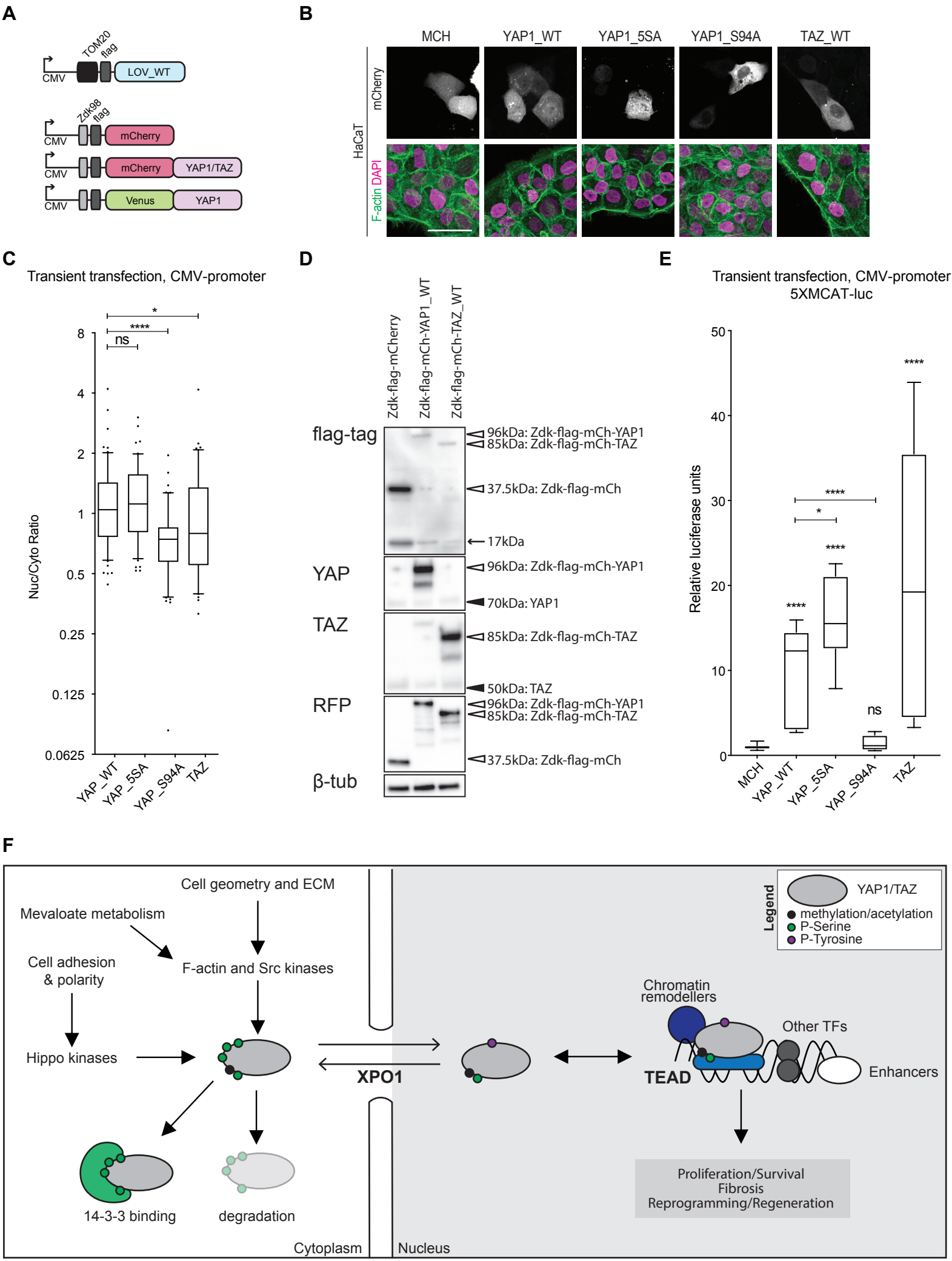

Supplementary Figure 2

A

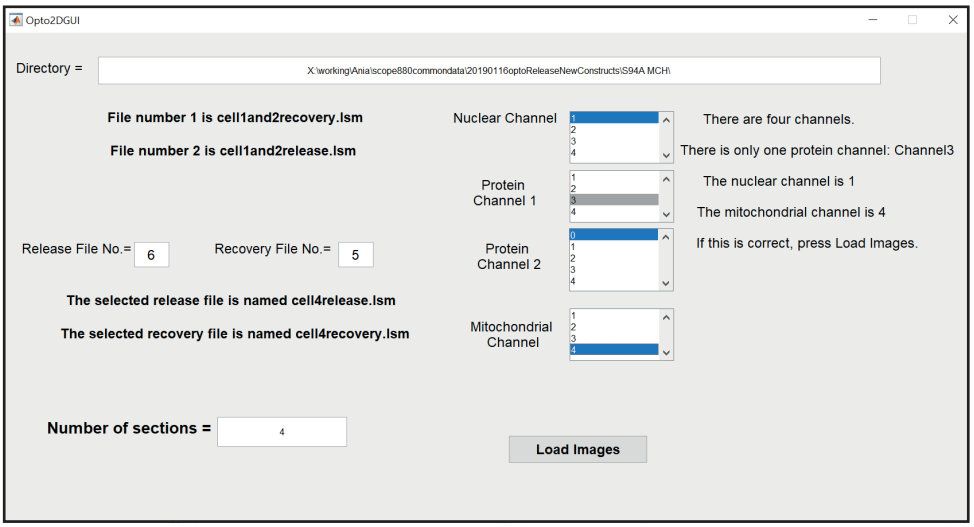

B

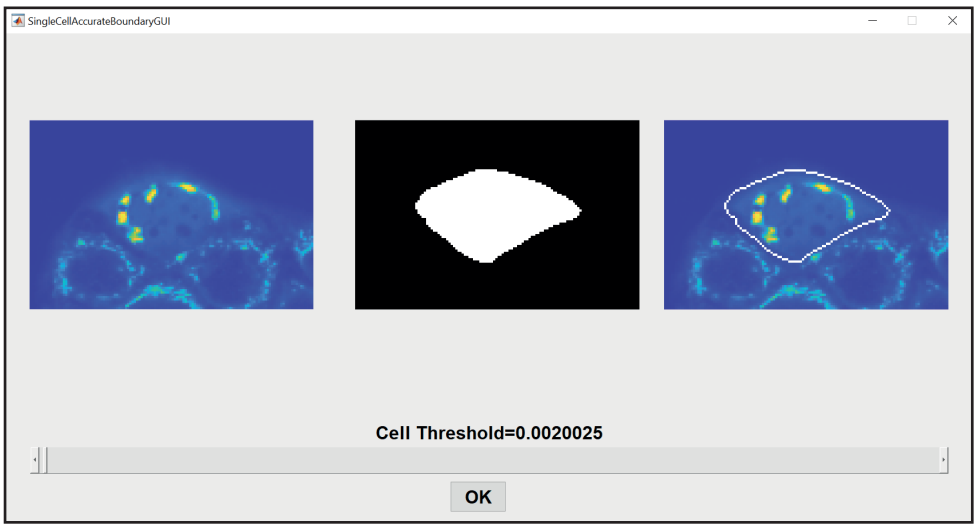

C

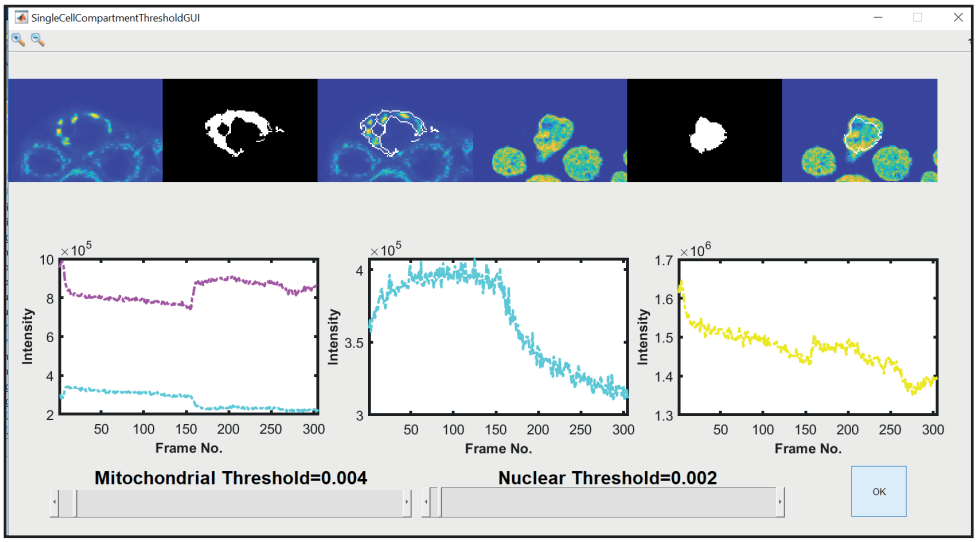

Supplementary Figure 3

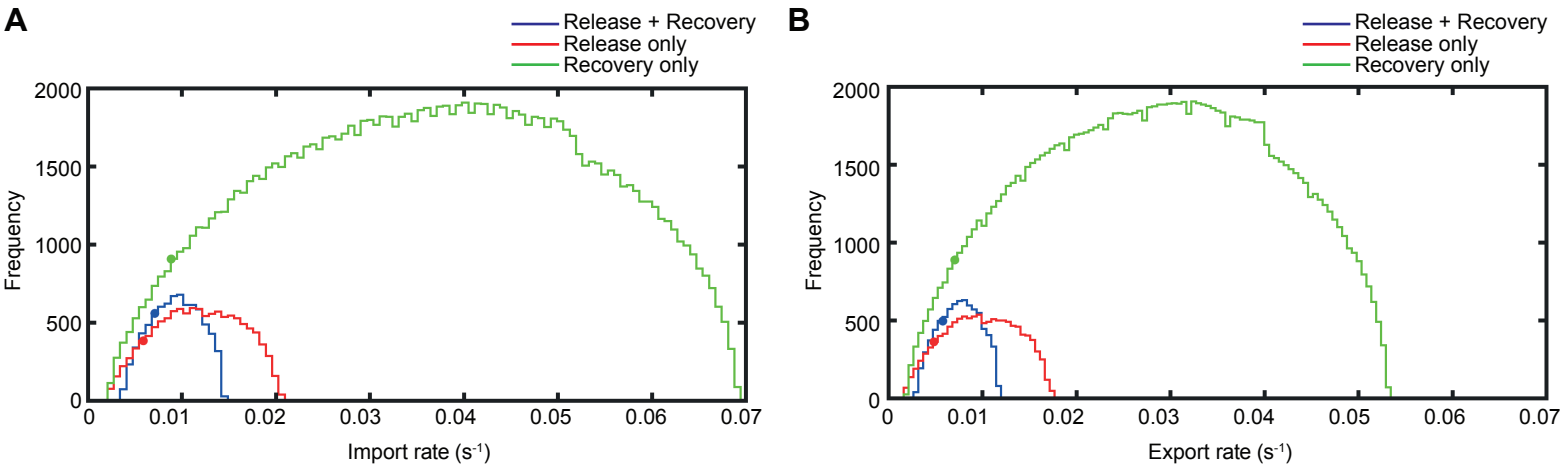

Supplementary Figure 4

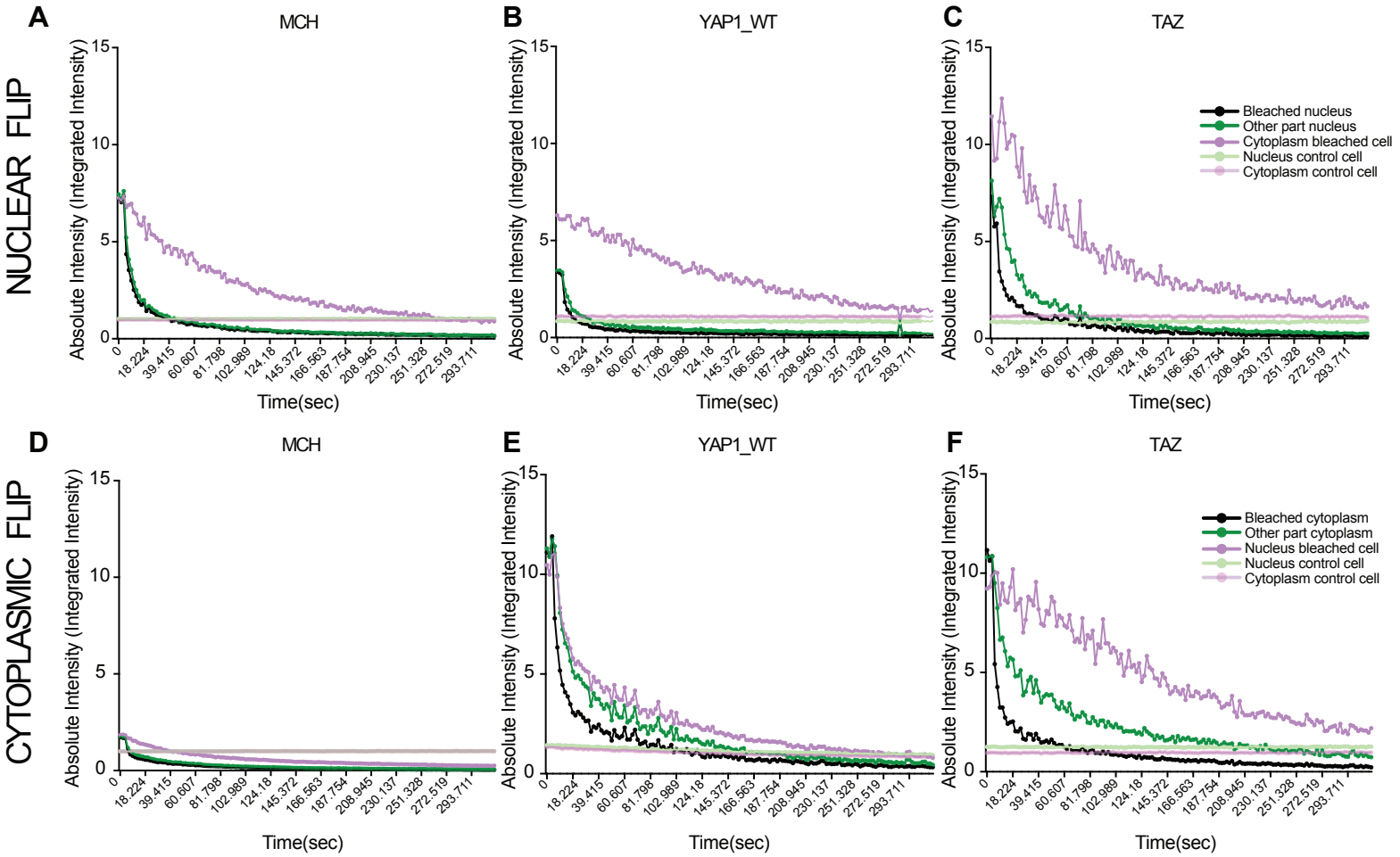

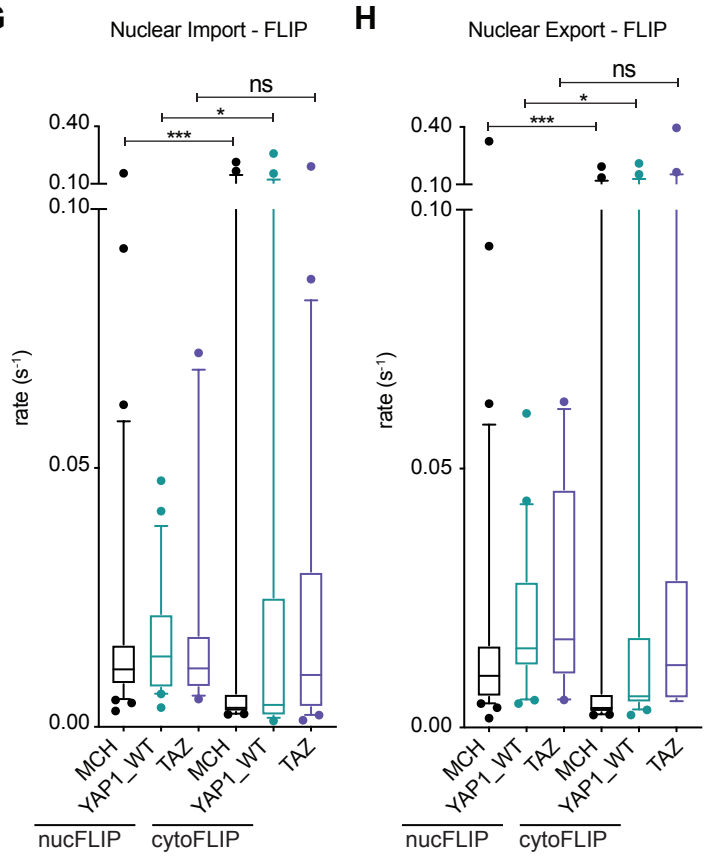

I

MEDIAN

	IMPORT (k_{in})			EXPORT (k_{out})		
construct	**Opto**	**FLIP nuc**	**FLIP cyto**	**Opto**	**FLIP nuc**	**FLIP cyto**
MCH	0.0015	0.0111	0.0037	0.0021	0.0100	0.0038
YAP1_WT	0.0029	0.0135	0.0042	0.0061	0.0153	0.0060
TAZ	0.0064	0.0113	0.0100	0.0146	0.0170	0.0120

Supplementary Figure 5

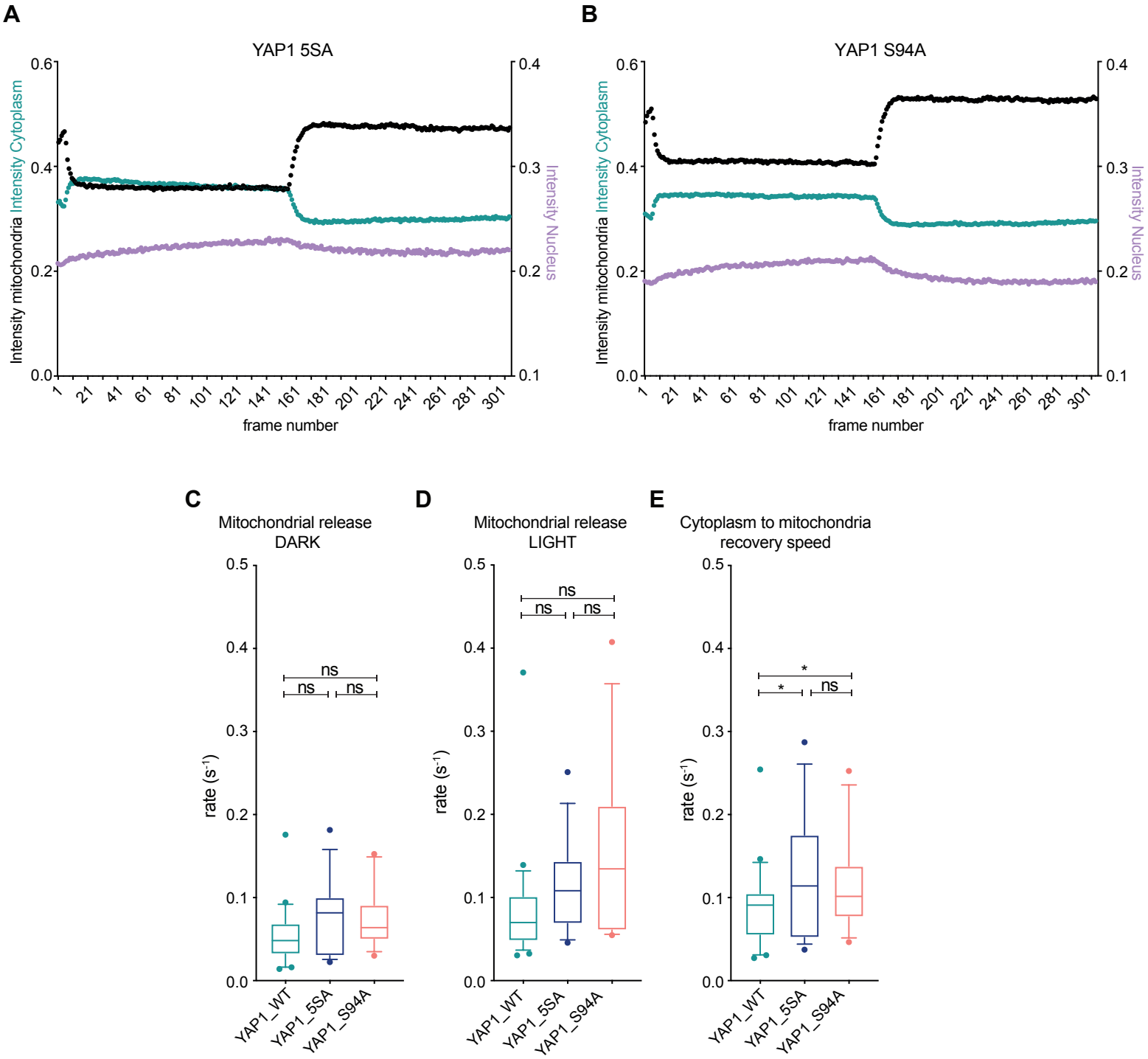

Supplementary Figure 6

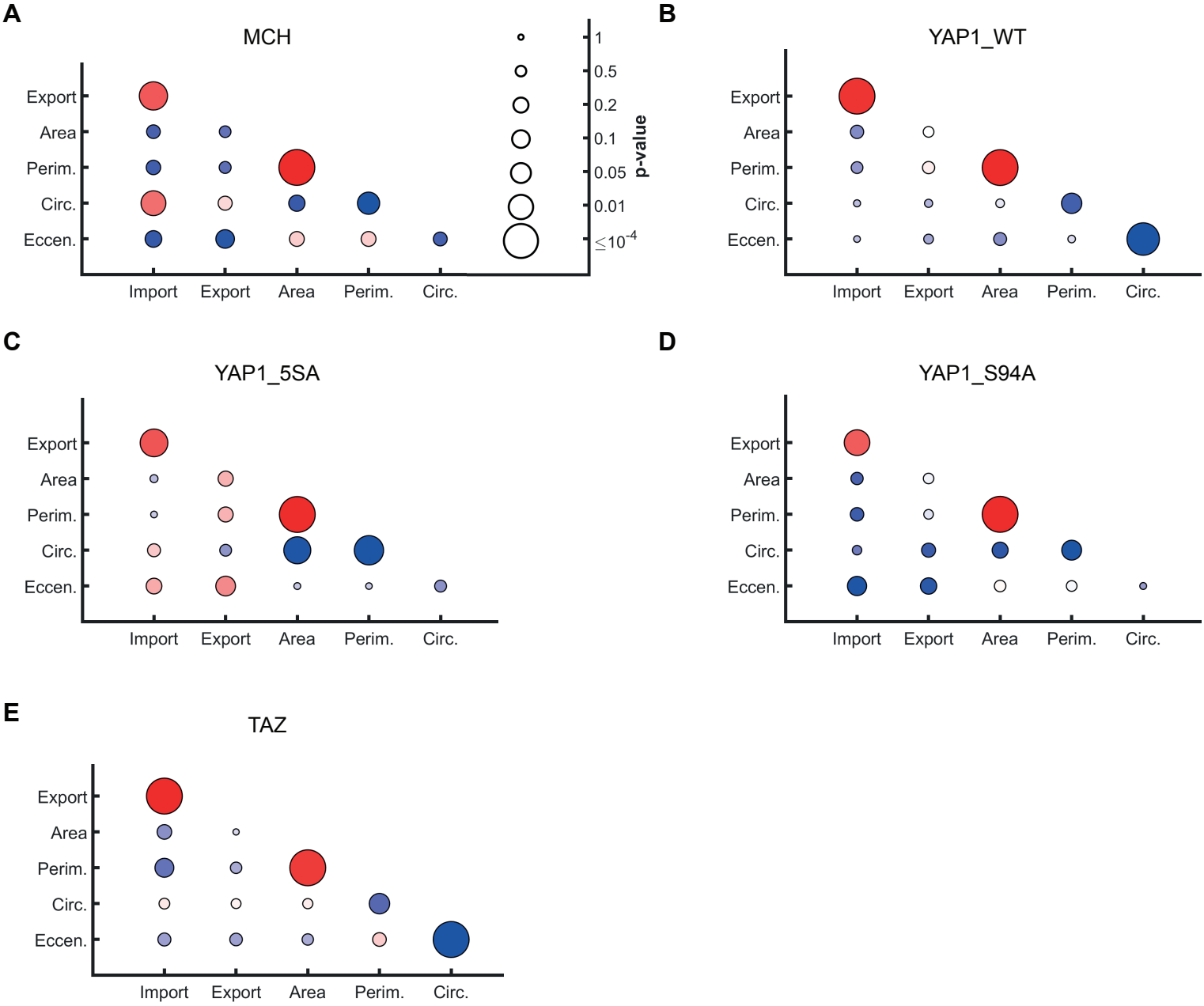
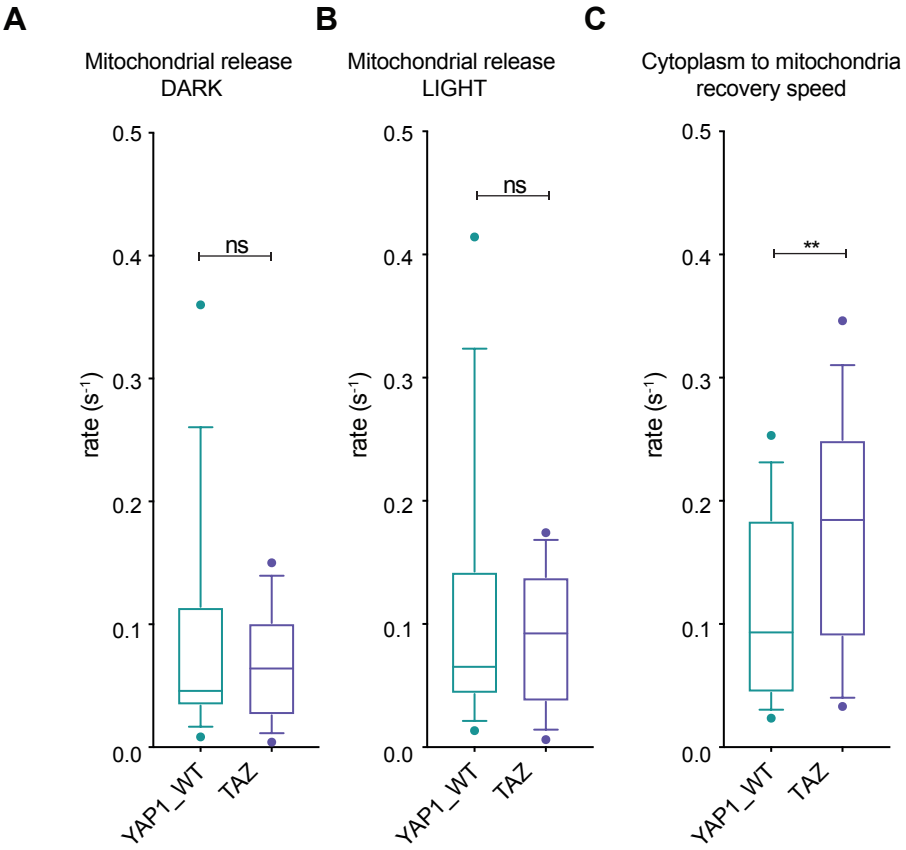
Supplementary Figure 7